International Journal of Thermal Sciences 157 (2020) 106514

Contents lists available at ScienceDirect

International Journal of Thermal Sciences

journal homepage: http://www.elsevier.com/locate/ijts

A phase change/metal foam heatsink for thermal management of battery packs

Ali Veismoradi [a], Alireza Modir [b], Mohammad Ghalambaz [c,d], Ali Chamkha [e,f,*]

[a] Chemical Engineering Department, Ferdowsi University, Mashhad, Iran
[b] Department of Mechanical and Material Engineering, Florida International University, Miami, FL 33174, United States
[c] Metamaterials for Mechanical, Biomechanical and Multiphysical Applications Research Group, Ton Duc Thang University, Ho Chi Minh City, Vietnam
[d] Faculty of Applied Sciences, Ton Duc Thang University, Ho Chi Minh City, Vietnam
[e] Institute of Research and Development, Duy Tan University, Da Nang 550000, Vietnam
[f] Institute of Theoretical and Applied Research (ITAR), Duy Tan University, Hanoi 100000, Vietnam

ARTICLE INFO

Keywords:
Battery pack
Melting/solidification phase change
Thermal energy storage
Metal-foam phase-change heat transfer

ABSTRACT

Heat transfer and phase change flow inside a Li-ion battery enclosure filled with a copper metal foam embedded in paraffin wax phase change material (PCM) are studied numerically. For simplicity and due to the axisymmetric of the enclosure geometry, half of the battery cell is considered as the heat source on the right wall. The vertical walls are considered symmetric, while the bottom wall is insulated, and the top wall is subjected to the convective heat transfer. The governing equations of the flow and heat transfer are presented as partial differential equations and then transformed into non-dimensional forms and solved by employing the finite element method. The local thermal equilibrium model was used, which limits the model to metal foams with high pore densities. For validation, results are compared with some of the well-known studies in the literature. The isotherms and streamlines are presented for three levels of heat pulse intensity. Both melting and solidification occur as a result of the unsteady heat pulses induced by the thermal source. The vertical location of the battery inside the enclosure can affect the streamlines and isotherm contours. Results show that for higher heat pulse powers, the melt volume fraction (MVF) increases, and heatsink will have higher efficiency. For a comparatively strong heat pulse, the efficiency was increased about seven times.

1. Introduction

Phase change materials (PCM) are capable of absorbing thermal energy and releasing that during the melting and solidification process to store energy. The advantages of PCMs such as low cost, high enthalpy, stable chemical characteristics, and temperature during phase change have gained attention for utilizing them in different industries. Phase change materials (PCM) are capable of thermal management, and energy storage are two applications of phase change materials [1]. PCMs have gained so much attention in applications such as energy-storing walls [2,3], passive heating systems in buildings [4], heat recovery by heat exchangers [5], solar energy [6], batteries [7] and also electronic cooling [8]. While these materials can store an enormous amount of thermal energy as the latent heat, the low thermal conductivity of them can be considered as a limitation for employing PCMs in industrial applications. Phase change heatsink, which requires fast thermal energy storage/release, is a well-known application of phase change materials. In a phase change heatsink, thermal shocks can be damped by storing/releasing extra thermal loads. The absorption of transient thermal loads in the heatsink requires an adequately high thermal response. Many studies [9,10] have been conducted for enhancing the thermal conductivity of PMCs and consequently improving the performance of phase change systems. Utilizing nanoparticles and porous materials with high thermal conductivity are two developing methods for increasing the thermal conductivity of PCMs.

Considering the heat transfer of PCMs in non-porous medium, Bondareva and Sheremet [11] numerically studied the melting of paraffin in a cubical cavity and compared the results for 2D and 3D cases. The results revealed the vital role of natural convection heat transfer in the liquid parts of the enclosure on the melting heat transfer. Bondareva and Sheremet [12] also investigated the unsteady heat transfer melting of a PCM in a two-dimensional cavity heated at the bottom by heating elements. They studied the formation and growth of convective circulation

* Corresponding author.
E-mail addresses: ali.veismoradi@mail.um.ac.ir (A. Veismoradi), amodi004@fiu.edu (A. Modir), mohammad.ghalambaz@tdtu.edu.vn (M. Ghalambaz), alichamkha@duytan.edu.vn (A. Chamkha).

https://doi.org/10.1016/j.ijthermalsci.2020.106514
Received 9 January 2020; Received in revised form 9 May 2020; Accepted 8 June 2020
Available online 7 July 2020

Nomenclature

Latin symbols

A_{mush}	a big numeric value of order 10^6
Bi	Biot number, $h_\infty H/k_{m,l}$
C_p	the specific heat capacity (J/(kg.K))
Da	Darcy number, κ/H^2
e	a small numeric value of order 10^{-3}
g	the gravity constant (m/s^2)
H	cavity size – geometrical scale characteristics
h	the coefficient of external convective heat transfer (W/(m^2.K^1))
h_{sf}	the fusion latent heat (J/kg)
k	coefficient of thermal conductivity (W/(m.K))
MVF	the scaled molten volume
n	the surface normal vector (m)
p	the pressure (N/m^2)
P	the dimensionless pressure
Pr	Prandtl number, $\nu/\alpha_{m,l}$
$q_0^{''}$	the heat flux (W.m^{-2})
Q''	the dimensionless heat flux
Ra	Rayleigh number, $(g\beta_l \Delta T H^3)/(\nu_l \alpha_{m,l})$
s	the source term of the enthalpy-porosity in the momentum equation
S	the dimensionless source term
Ste	Stefan number, $((\rho C_p)_{m,l}\ \Delta T)/(\rho_l h_{sf,m})$
t	the dimensional time (s)
T	the temperature field (K)
u, v	the velocity in the x and y directions (m/s)
U, V	the dimensionless velocity in the X and Y -directions
x, y	the x and y -coordinates (m)
X, Y	the dimensionless X and Y –directions

Greek symbols

α	the coefficient of the thermal diffusivity (m^2/s)
β	the coefficient of volumetric thermal expansion (1/K)
δt	the heat pulse duration (s)
δT	the temperature bond of the phase change (K)
ΔT	the temperature scale (K), $q''_o H/k_{m,l}$
$\delta\tau$	non-dimensional heat pulse duration
ε	porosity of the metal foam
η	heatsink efficiency
θ	non-dimensional temperature
κ	permeability of the metal foam (m^2)
λ	the intensity of the heating pulse power
μ	the dynamic viscosity (kg/(m.s))
ν	the kinematic viscosity (m^2/s)
ξ	the power of heat load, the basis function of the finite element method
ρ	density (kg/m^3)
τ	the non-dimensional time
φ	the melt volume fraction

Subscripts

0	start of heat pulse
1	end of heat pulse
∞	the external cooling flow
ave	average
b	bottom wall
f	fusion
l	liquid/molten PCM
m	effective of the PCM and porous matrix
s	solid PCM

cells by increasing the heat generation of the thermal source. Kumar et al. experimentally studied the melting of lead in a scaled cuboid with constant heat flux at one [13] and two [14] vertical walls while the horizontal walls were insulated. They compared the solid-liquid interface at different time steps during the melting by using different methods. Bertrand et al. [15] numerically studied the laminar melting of a pure substance in a 2D cavity. The filled material considered to be initially solid and increasing the temperature of one of the vertical walls triggered the melting process.

Nanoparticle addition for the purpose of increasing the thermal conductivity of phase change materials has been studied extensively by many researchers [16–18]. Ghalambaz et al. [19,20] addressed the effect of using nano-encapsulated phase change materials in the convection heat transfer. Bondareva et al. [21] simulated the heat transfer inside a 2D rectangular cavity with internal fins filled with paraffin and nanoparticles. The results were presented for different inclination angles of the cavity and different nanoparticle concentrations. Results revealed that the presence of nanoparticles accelerates the heat transfer inside the enclosure in all inclination angles. In another study, Bondareva et al. [22] studied the effect of radiator fin height and nanoparticle concentration. Many researchers have studied the effect of utilizing hybrid nanoparticle [23,24], simple nanoparticles [18,25,26], presence of fins with different geometry [27] and magnetic field on the heat transfer of PCMs in enclosures. Results revealed that the addition of nanoparticles could enhance or decrease the phase change rate based on the kind of nanoparticles, the geometry of the enclosure, and the type of employed phase change material. While the presence of a magnetic field generally represses the natural convection and results in heat transfer reduction in the cavity. There are also excellent reviews on the thermal behavior of nanoparticle additives [28,29].

Employing porous materials with high thermal conductivity is another method for increasing the heat transfer in cavities. Sivasankaran et al. [30] studied the heat transfer in an enclosure with a heat-generating porous medium filled with water-based nanofluid and copper nanoparticles. The results indicate that the average Nusselt number and, consequently, the heat transfer in the enclosure increases with increasing the porosity of the metal foam. Ghalambaz et al. [31] examined the heat transfer in a porous cavity with hot and cold elements positioned at various locations on vertical walls. The results indicate that the natural convection heat transfer in the porous cavity is significantly influenced by the location of the hot and cold elements. Paknezhad et al. [32] experimentally examined the effect of an aluminum metal foam, as a heatsink, on free convection heat transfer for a heater at different inclination angles. The maximum thermal efficiency, 17%, reported when the metal foam was positioned vertically. Various papers in the literature considered different parameters in the heat transfer in porous media, including cavity boundary conditions [33], double-diffusive natural convection [34] and cavities with a partially filled porous layer [35–37].

Phase change heat transfer in porous media is an interesting topic, and only a few researchers have focused on this problem. Xiao et al. [38] used the vacuum impregnation method for the preparation of paraffin/metal foam composite PCMs with more than 90% porosity. Copper and Nickel are the two metals used in the sample preparation experiment. The thermophysical measurements of the samples showed significant growth in the thermal conductivity of the composite PCMs. Paraffin/copper foam composite showed 15 times higher thermal conductivity in comparison with the pure paraffin. In another experimental study, Zheng et al. [39] investigated the changes in the melting behavior of paraffin when using copper metal foam. Results revealed that copper

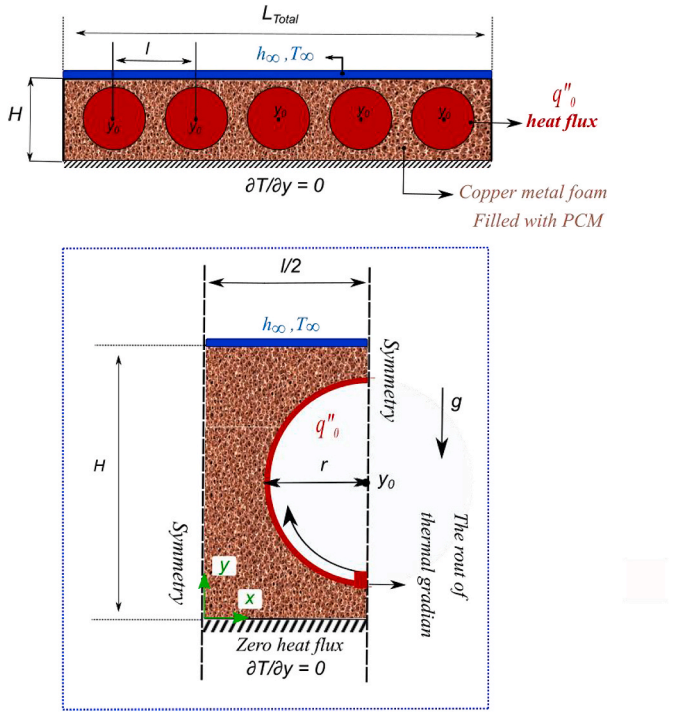

Fig. 1. Schematic representation of heatsink packed with copper-foam and PCM.

foam/paraffin PCM melts 20.5% faster compared to pure paraffin, which means a reduction in thermal resistance of paraffin due to copper foam addition.

Hossain et al. [40] numerically investigated the thermal performance of an enclosure filled with a phase change material (Cyclohexane), a porous medium (Aluminum foam), and also nano-enhanced PCM with CuO nanoparticles. Al-Jethelah et al. [41] studied the effect of employing nanoparticles on heat transfer of PCM inside a square cavity filled with a porous medium. The left wall of the cavity was heated, and other walls were thermally isolated. The results confirmed the increase of PCM thermal conductivity with the addition of nanoparticles. Although adding nanoparticles increases the viscosity of the PCM, it does not suppress the natural convection currents in the enclosure.

All the studies mentioned above considered a steady thermal load, while in different real-world situations, thermal load is unsteady. The charging and discharging process in lithium-ion batteries is an example of unsteady thermal loading. Hussain et al. [42] used a metal foam/-paraffin composite in lithium-ion batteries and compared the experimental results with a pure PCM and natural air cooling. The battery surface temperature decreased by 31% and 24% compared to pure PCM and natural air cooling systems, respectively. Very recently, Ghalambaz and Zhang [43] modeled the transient phase change of PCMs, embedded in metal foams, in an annulus space heatsink for a single battery application. The outcomes show that the fusion temperature of PCM is an essential parameter on the thermal behavior of the heatsink. Ling et al. [44] experimentally investigated the benefit of using a phase change heatsink for thermal management of a battery pack by using composite phase change materials. They reported that the thermal conductivity of the PCM is the essential factor for the uniform temperature of the batteries during the charging and discharging cycles.

As mentioned in the literature review, there have been some recent theoretical studies on phase-change heat transfer analysis of PCM-metal foams subjected to steady heat loads, in which the focus was either on melting [40,41] or solidification [45]. When transient heat loads are applied in a phase-change heat transfer process, both melting and solidification will occur due to the nature of thermal loads and external cooling. Following the experimental research in Ref. [42] and theoretical study of [43], this paper, for the first time, examines the phase change behavior of PCMs-metal foams in a cavity with a heat pulse thermal load for thermal management of batteries-pack applications.

1.1. Mathematical model

The 2D enclosure illustrated in Fig. 1(a), represents a simple model of a Li-ion battery pack with five cells, considered in this study. Here, l is the center-to-center distance of the battery cells. As shown in Fig. 1(b), due to the symmetry, a section of the battery with a width of $l/2$ is selected for the mathematical model. The cavity is packed with copper metal foam, which is considered homogeneous with the permeability of κ and the porosity of ε. The heatsink enclosure and the porous space is filled with paraffin-wax phase change material with the fusion temperature of T_f. The bottom-wall of the heatsink is insulated, and the top wall is subjected to a convective heat transfer h_∞ with the surroundings temperature T_∞ ($T_\infty < T_f$).

The semicircular boundary on the right side of the enclosure considered as a pulse heat flux with the base power of q''_0 and in a time interval of δt it raises to the value of $(1+\gamma)\, q''_0$. After an adequately long time, the heat flux reduces to q''_0. Initially, the PCM is at the ambient temperature (T_∞), and the heatsink reaches a steady-state condition after the increase in the heat flux for a sufficiently long time. Then suddenly, the heat flux rises to the high heat flux of $(1+\gamma)\, q''_0$ during t_0 to t_1 (a time interval of δt) starting at t_0. At t_1, the heat flux reduces back to the base heat flux.

1.2. Governing equations

According to the abovementioned assumptions, the set of governing equation for two-dimensional molten PCM flow and heat transfer in the free layer and porous medium layer can be written as follows [46,47]:

$$\frac{\partial u}{\partial x}+\frac{\partial v}{\partial y}=0 \tag{1}$$

$$\frac{\rho_l}{\varepsilon}\frac{\partial u}{\partial t}+\frac{\rho_l}{\varepsilon^2}\left(u\frac{\partial u}{\partial x}+v\frac{\partial u}{\partial y}\right)=-\frac{\partial p}{\partial x}+\frac{\mu_l}{\varepsilon}\left(\frac{\partial^2 u}{\partial x^2}+\frac{\partial^2 u}{\partial y^2}\right)-\frac{\mu_l}{\kappa}u-s(T)u \tag{2}$$

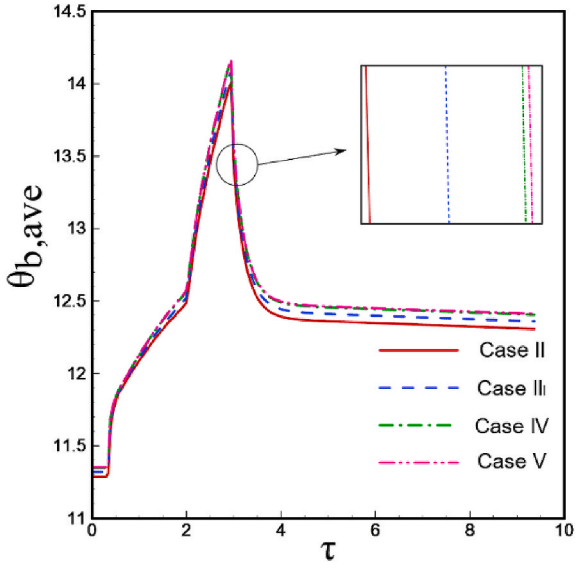

Fig. 2. The influence of the mesh size on the hot-element average temperature ($\theta_{b,\,ave}$) as a function of τ

Table 1
The thermos-physical properties paraffin wax (PCM) and of copper foam (porous medium) [39].

Material	ρ (kg/m^3)	c_p (J/kg.K)	k (W/m.K)	μ (Pa.s)	h_{sf} (J/kg.K)	B (1/K)
Copper foam	8900	386	380	–	148800	–
Paraffin	900	2300	0.3	0.00324	–	0.0005

$$\frac{\rho_l}{\varepsilon}\frac{\partial v}{\partial t}+\frac{\rho_l}{\varepsilon^2}\left(u\frac{\partial v}{\partial x}+v\frac{\partial v}{\partial y}\right)=-\frac{\partial p}{\partial y}+\frac{\mu_l}{\varepsilon}\left(\frac{\partial^2 v}{\partial x^2}+\frac{\partial^2 v}{\partial y^2}\right)-\frac{\mu_l}{\kappa}v-s(T)v+\beta_l\rho_l g\left(T-T_f\right) \tag{3}$$

Energy balance in metal foam as:

$$\left(\rho C_p\right)_m\frac{\partial T}{\partial t}+\left(\rho C_p\right)_l\left(u\frac{\partial T}{\partial x}+v\frac{\partial T}{\partial y}\right)=k_m\left(\frac{\partial^2 T}{\partial x^2}+\frac{\partial^2 T}{\partial y^2}\right)-\varepsilon\rho_l h_{sf}\frac{\partial\varphi(T)}{\partial t} \tag{4}$$

where $(\rho C_p)_m = \varphi(\rho C_p)_{m,l} + (1-\varphi)(\rho C_p)_{m,s}$, in which, $(\rho c)(\rho c)_{m,l} = (1-\varepsilon)(\rho C_p)_p + \varepsilon(\rho C_p)_l$, $(\rho c)(\rho c)_{m,s} = (1-\varepsilon)(\rho C_p)_p + \varepsilon(\rho C_p)_s$. For the thermal equation, the local thermal equilibrium between the metal foam and PCM was assumed. This means that the temperature of the porous l matrix and the PCM inside the pores is locally the same. This assumption is valid when there is high hydraulic interaction between the porous matrix and the PCM in the pores. The number of pores density is also an important factor for this assumption. As discussed in Ref. [48], when the number of pores per inch is high, then the local thermal assumption can be considered valid. As a result, the outcomes of the present study are limited to the case of metal foams with high pore densities.

Here, permeability and porosity of the metal foam are denoted as κ and ε, respectively. ρ is the density, μ is the dynamic viscosity, β is the coefficient of volumetric thermal expansion, C_p is the specific heat capacity, and φ is the melt volume fraction. k is the thermal conductivity, and h_{sf} is the latent heat of fusion. The subscripts used in these equations are p, l, s, and m, which denote the porous matrix, liquid PCM, solid PCM, and the effective properties, respectively.

Here, the molten volume fraction is denoted as φ, and the effective heat capacity $(\rho C_p)_m$ in the liquid and solid-state can be evaluated as $(\rho C_p)_m = (1-\varphi)(\rho C_p)_{m,s} + \varphi(\rho C_p)_{m,l}$. Accordingly, the effective heat capacity at the liquid and solid statuses of PCM are evaluated as $\rho C_p)_{m,l} = (1-\varepsilon)(\rho C_p)_l + \varepsilon(\rho C_p)_l$ and $(\rho C_p)_{m,s} = (1-\varepsilon)(\rho C_p)_s + \varepsilon(\rho C_p)_l$, respectively.

For computing the effective thermal conductivity of the metal foam and embedded PCM, one can use the available models in the literature or extract it directly from the experimental data. Many of the relations are discussed in the comprehensive review study of Ranut [49]. The most commonly used equation in the literature is expressed in Ref. [39,50]. In the present study, the experimental data of Xiao et al. [38] for the properties of paraffin/copper foam composite are used directly.

Table 2
The list of the thermophysical properties.

Property [Unit]	Symbol	Value
Density of liquid PCM [kg/m^3]	ρ_l	900
Dynamic viscosity of the liquid PCM [kg/(m s)]	μ_l	0.00324
Effective heat capacity of PCM and porous matrix [J/(m^3 K)]	$(\rho C_{p,m})_l$	2.0445×10^6
Effective thermal conductivity of PCM and metal foam [W/(m K)]	$K_{l,m}$	4.8
Effective thermal diffusivity of PCM and porous matrix [m^2/s]	$\alpha_{l,m}$	2.3478×10^{-6}
Heat capacity of PCM [J/(m^3 K)]	$(\rho C_p)_l$	2.07×10^6
Specific heat capacity of PCM [J/(kg K)]	Cp_l	2300
Thermal conductivity of PCM [W/(m K)]	K_l	0.3
Thermal expansion coefficient of PCM [1/K]	β_l	0.0005

Table 3
The dependency of the $\theta_{b,\ ave}$ and $\varnothing_{b,ave}$on the grid size.

Case	Number of Element	$\theta_{b,\ ave}$	*MVF*
Case I	282	11.340	0.19684
Case II	550	11.354	0.21767
Case III	882	11.360	0.22608
Case IV	1746	11.365	0.23278
Case V	2229	11.366	0.23410
Case VI	2729	11.366	0.23493

The source term $s(T)$ in Eq. (2) and Eq. (3) controls the momentum equation in liquid and solid regions. The $s(T)$ term, which is defined in Eq. (5), increases abruptly in a solid region, which causes a tremendous reduction in the velocity component. It is in the form of Darcy term and vanishes in the liquid region [23,46].

$$s(T)=A_{mush}\frac{(1-\varphi(T))^2}{\varphi(T)^3+e} \tag{5}$$

Here A_{mush} *is* a big numeric value of order 10^6 and higher. Here, φ (T) is the molten volume fraction and is defined as below:

$$\varphi(T)=\begin{cases}0 & T<T_f\\ \dfrac{T-T_f}{\delta T} & T_f<T<T_f+\delta T\\ 1 & T>T_f+\delta T\end{cases} \tag{6}$$

In Eq. (6), the assumption is that the phase change takes place at the small thermal steps of δT, and φ (T) varies linearly with the temperature. Paraffin is considered fully liquid ($\varphi = 1$) or fully solid ($\varphi = 0$) outside the fusion temperature range. The energy storage/released during the phase change is controlled by $\partial\varphi/\partial t$ source term in Eq. (4). It is multiplied by ε (the porosity of the metal foam), indicating that only the existing PCM in the pores undergoes the phase change, not the porous matrix. Also, for helping the stability and convergence of the solution, viscosity is artificially introduced as a function of molten volume fraction as $\mu_l(\varphi) = \mu_l + (1-\varphi)$. This function reduces to the regular value of μ_l in a liquid region ($\varphi = 1$) and in a solid region ($\varphi = 0$) the artificial viscosity increases to a large value of $\mu_l(\varphi) = \mu_l + 1$. This will decrease the velocity components in the momentum equation to zero.

The boundary conditions associated with the physical model shown in Fig. 1 is listed below.

The left and right walls are symmetric as

$$\frac{\partial T}{\partial x}=0\ and\ \frac{\partial u}{\partial x}=0 \tag{7a}$$

The bottom wall is adiabatic as

$$\frac{\partial T}{\partial y}=0 \tag{7b}$$

The top wall is subject to convective heat transfer as

$$k_m\frac{\partial T}{\partial y}=h_\infty(T-T_\infty) \tag{7c}$$

The circular battery shell is subjected to a transient heat flux with the power of $q"_0$.

$$k_m\frac{\partial T(x,0)}{\partial y}=q''_0 \tag{7d}$$

Impermeability and no-slip condition are considered for fluid flow on the wall and melting interface. The pressure point of zero was assumed as a reference in the middle of the circular shell. It was assumed that initially, the element is off, and the enclosure is at the uniform temperature of T_∞. When the battery is under operation, the heat flux with the power of q''_0 is considered for a sufficiently long time until heatsink reaches a steady-state condition. Accordingly, the initial condition of results is accomplished when the regular q''_0 is applied.

Eqs. (1)–(7) are expressed in non-dimensional forms using the following dimensionless variables:

$$X=\frac{x}{H},\ Y=\frac{y}{H},\ U=\frac{uH}{\alpha_{m,l}},\ V=\frac{vH}{\alpha_{m,l}},\ \theta=\frac{T-T_\infty}{\Delta T},$$
$$\tau=\frac{t\alpha_{m,l}}{H^2},\ S(\theta)=\frac{s(T)H^2}{\rho_l\alpha_{m,l}},\ P=\frac{pH^2}{\rho\alpha_{m,l}{}^2},\ \alpha_{m,l}=\frac{k_{m,l}}{(\rho c_p)_{m,l}},$$
$$\Pr=\frac{\nu}{\alpha_{m,l}},\ Ra=\frac{g\beta_l\Delta TH^3}{\nu_l\alpha_{m,l}},\ Ste=\frac{(\rho Cp)_{m,l}\Delta T}{\rho_l h_{sf}},\ Da=\frac{\kappa}{H^2} \tag{8}$$

Here, H is the characteristic length which is equal to the height of the cavity, Ra and Pr are the Rayleigh and Prandtl numbers, respectively. The temperature difference is defined as $\Delta T=q''H/k_{m,l}$ where $k_{m,l}$ is the effective thermal conductivity of the liquid PCM filled in the porous medium. The Rayleigh- Darcy number can be introduced as $RD=Da\times Ra$ as the actual power of convection heat transfer.

The non-dimensional form of Eqs. (1)–(7) are obtained and listed below by substituting Eq. (8) into them.

Continuity:

$$\frac{\partial U}{\partial X}+\frac{\partial V}{\partial Y}=0 \tag{9}$$

Momentum in x-direction:

$$\frac{1}{\varepsilon}\frac{\partial U}{\partial\tau}+\frac{1}{\varepsilon^2}\left(U\frac{\partial U}{\partial X}+V\frac{\partial U}{\partial Y}\right)=-\frac{\partial P}{\partial X}+\frac{\Pr}{\varepsilon}\left(\frac{\partial^2U}{\partial X^2}+\frac{\partial^2U}{\partial Y^2}\right)-\frac{\Pr}{Da}U-S(\theta)U \tag{10a}$$

Momentum in y-direction:

$$\frac{1}{\varepsilon}\frac{\partial V}{\partial\tau}+\frac{1}{\varepsilon^2}\left(U\frac{\partial V}{\partial X}+V\frac{\partial V}{\partial Y}\right)=-\frac{\partial P}{\partial Y}+\frac{\Pr}{\varepsilon}\left(\frac{\partial^2V}{\partial X^2}+\frac{\partial^2V}{\partial Y^2}\right)-\frac{\Pr}{Da}V-S(\theta)V+\Pr Ra\theta \tag{10b}$$

The geometrical non-dimensional parameters are $L=l/H$, $R=r/H$ and E_C=(y_0-H/2)/H. Where E_C is the non-dimensional location of battery shell (hot cylinder).

Energy balance for melted PCM:

$$\left(\varphi+(1-\varphi)\frac{(\rho Cp)_{m,s}}{(\rho C_p)_{m,l}}\right)\frac{\partial\theta}{\partial\tau}+\left(\frac{(\rho C_p)_{m,l}}{(\rho C_p)_l}\right)^{-1}\left(U\frac{\partial\theta}{\partial X}+V\frac{\partial\theta}{\partial Y}\right)$$
$$=\frac{k_m}{k_{m,l}}\left(\frac{\partial^2\theta}{\partial X^2}+\frac{\partial^2\theta}{\partial Y^2}\right)-\frac{1}{Ste}\frac{\partial\varphi(\theta)}{\partial\tau} \tag{11}$$

where Ste is the Stephan number.

The bottom wall is adiabatic as

$$\frac{\partial\theta}{\partial Y}=0 \tag{12}$$

The top wall is subject to convective heat transfer as

$$\left(\frac{k_m}{k_{m,l}}\right)\frac{\partial\theta}{\partial Y}=Bi\theta_\infty \tag{13}$$

where Bi = $h_\infty H/k_{m,l}$. The battery shell is subjected to a uniform heat flux as:

$$\left(\frac{k_m}{k_{m,l}}\right)\frac{\partial\theta(X,0)}{\partial X}=1 \tag{14}$$

The non-dimensional thermophysical properties can be summarized as:

$$\frac{k_{m,s}}{k_{m,l}}\sim 1,\ \frac{(\rho C_p)_{m,s}}{(\rho C_p)_{m,l}}=\frac{(1-\varepsilon)(\rho C_p)_p+\varepsilon(\rho C_p)_s}{(1-\varepsilon)(\rho C_p)_p+\varepsilon(\rho C_p)_l}\sim 1 \tag{15}$$

$$\varphi(\theta)=\begin{cases}0 & \theta<\theta_f\\ \dfrac{\theta-\theta_f}{\delta\theta} & \theta_f<\theta<\theta_f+\dfrac{\delta T}{\Delta T}\\ 1 & \theta>\theta_f+\dfrac{\delta T}{\Delta T}\end{cases} \tag{16}$$

where θ_f= (T_f-T_∞)/ΔT.

In this study, following the experimental study in Ref. [38], the porosity value, ε, is considered to be 0.975 for 5 PPI porous pores. The permeability is adopted from Ref. [51] as 2.7 × 10^{-7} m^2. The effective thermal conductivity of the copper foam and the paraffin wax is adopted as k_m = 4.8 W/m.K.

The dimensionless temperature of the battery shell, which is defined as bellow, is the characteristic parameter in this paper.

$$\theta_b=\frac{T_b-T_\infty}{\Delta T}\ \ at\ Y=0 \tag{17}$$

And the average battery shell temperature can be calculated as:

$$\theta_{b,ave}=\frac{\int_0^{L_h}\theta_b}{L_h} \tag{18}$$

The energy balance at the semi-circular shell surface, while there is no pulse, can be written as:

$$q''(t)\times H=H\times h_\infty(T_b-T_\infty) \tag{19}$$

In a non-dimensional form, it can be written as follows

$$\theta_{b,0}=\frac{1+\gamma(\tau)}{Bi} \tag{20}$$

Therefore, the heatsink efficiency can be calculated as:

$$\eta=\frac{1+\gamma(\tau)}{Bi\theta_{b,ave}} \tag{21}$$

Finally, the melting volume fraction is introduced as:

$$MVF=\frac{\int_A\varepsilon\varphi dA}{\int_A\varepsilon dA} \tag{22}$$

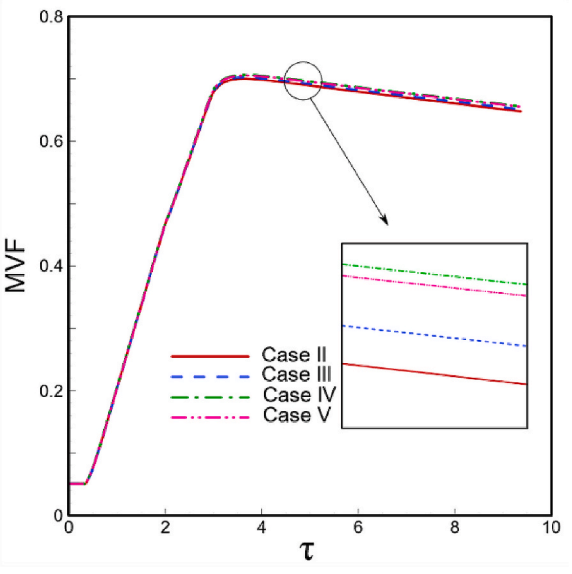

Fig. 3. Mesh size effect on the time history of normalized melt volume fraction.

$$R_i^2 \approx \frac{1}{\varepsilon}\sum_{m=1}^{N} V_m \int \frac{\partial \gamma_m}{\partial \tau}\gamma_i dXdY + \frac{1}{\varepsilon^2}\sum_{m=1}^{N} V_m \int \left[\left(\sum_{m=1}^{N} U_m\gamma_m\right)\frac{\partial \gamma_m}{\partial X} + \left(\sum_{k=1}^{N} V_m\gamma_m\right)\frac{\partial \gamma_m}{\partial Y}\right]\gamma_i dXdY$$
$$+\sum_{m=1}^{N}\int\left(-\sum_{m=1}^{N} P_m\gamma_m\right)\frac{\partial \gamma_i}{\partial Y}dXdY + A(\varphi)\frac{2Pr}{\varepsilon}\sum_{m=1}^{N} V_m\int\frac{\partial \gamma_m}{\partial Y}\frac{\partial \gamma_i}{\partial Y}dXdY$$
$$+A(\varphi)\frac{Pr}{\varepsilon}\sum_{m=1}^{N} U_m\int\left[\frac{\partial \gamma_m}{\partial Y}\frac{\partial \gamma_i}{\partial X}\right]dXdY + A(\varphi)\frac{Pr}{\varepsilon}\sum_{m=1}^{N} V_m\int\frac{\partial \gamma_m}{\partial X}\frac{\partial \gamma_i}{\partial X}dXdY$$
$$-A(\varphi)\frac{Pr}{Da}\int\left(\sum_{m=1}^{N} V_m\gamma_m\right)\gamma_i dXdY - S(\theta)\int\left(\sum_{m=1}^{N} V_m\gamma_m\right)\gamma_i dXdY + PrRa\int\left(\sum_{m=1}^{N}\theta_m\gamma_m\right)\gamma_i dXdY \quad (25)$$

1.3. Numerical method

In the first step, the non-dimensional partial differential equations 9–11 plus the associated boundary condition (12)–(14) were converted to the weak form. These equations are then solved employing Galerkin finite element method [52,53]. In order to satisfy the mass conservation,

$$R_i^3 \approx \sum_{m=1}^{N} U_m\int\frac{\partial \gamma_m}{\partial X}\gamma_i dXdY + \sum_{m=1}^{N} V_m\int\frac{\partial \gamma_m}{\partial Y}\gamma_i dXdY \quad (26)$$

$$R_i^4 \approx \left(\varphi + (1-\varphi)\frac{(\rho Cp)_{m,s}}{(\rho C_p)_{m,l}}\right)\sum_{m=1}^{N}\theta_m\int\frac{\partial \gamma_m}{\partial \tau}\gamma_i dXdY$$
$$+\left(\frac{(\rho C_p)_{m,l}}{(\rho C_p)_{l}}\right)^{-1}\sum_{m=1}^{N}\theta_m\int\left[\left(\sum_{m=1}^{N} U_m\gamma_m\right)\frac{\partial \gamma_m}{\partial X} + \left(\sum_{m=1}^{N} V_m\gamma_m\right)\frac{\partial \gamma_m}{\partial Y}\right]\gamma_m dXdY$$
$$+\frac{k_m}{k_{m,l}}\sum_{m=1}^{N}\theta_k\int\left[\frac{\partial \gamma_m}{\partial X}\frac{\partial \gamma_i}{\partial X} + \frac{\partial \gamma_m}{\partial Y}\frac{\partial \gamma_i}{\partial Y}\right]dXdY - \frac{1}{Ste}\sum_{m=1}^{N}\frac{\partial \varphi(\theta_m)}{\partial \theta}\int\frac{\partial \gamma_m}{\partial \tau}\gamma_i dXdY \quad (27)$$

the continuity equation (9) is utilized in Eq. (26), which will be used to control the pressure distribution.

Within the domain interval of $0 < X < 0.5$ and $0 < Y < 1$, the temperature, θ, and the x and y velocity components (u and v) are expanded calling a basis set $\{\gamma_k\}_{k=1}^{N}$ as:

$$P \approx \sum_{m=1}^{N} P_m\gamma_m(X,Y), U \approx \sum_{m=1}^{N} U_m\gamma_m(X,Y), V \approx \sum_{m=1}^{N} V_m\gamma_m(X,Y), \theta \approx \sum_{m=1}^{N}\theta_m\gamma_m(X,Y) \quad (23)$$

In the governing equations, Eqs. (24)–(27), the nonlinear residual equations ($R^1{}_i$, $R^2{}_i$, $R^3{}_i$ and $R^4{}_i$) can be reproduced by employing the basis functions presented in Eq. (23).

Free step Backward Differentiation Formula (BDF) as an automatic time-step method is employed to control the computational error by adjusting the time steps within a variable order scheme between one and two [54]. The Newton method, using the PARDISO solver [55–57], is adopted to iteratively solve the residual Eqs. (27)-(30) with a residual error O (10^{-5}). The damping factor of the Newton method is fixed as 0.8. The computations were performed using the SUNDIALS solver [58].

1.4. Non-dimensional parameters

As it is shown in Fig. 1, a 10 cm high cavity, which is filled with a

$$R_i^1 \approx \frac{1}{\varepsilon}\sum_{m=1}^{N} U_m\int\frac{\partial \gamma_m}{\partial \tau}\gamma_i dXdY + \frac{1}{\varepsilon^2}\sum_{m=1}^{N} U_m\int\left[\left(\sum_{m=1}^{N} U_m\gamma_m\right)\frac{\partial \gamma_m}{\partial X} + \left(\sum_{k=1}^{N} V_m\gamma_m\right)\frac{\partial \gamma_m}{\partial Y}\right]\gamma_i dXdY$$
$$+\sum_{m=1}^{N}\int\left(-\sum_{m=1}^{N} P_m\gamma_m\right)\frac{\partial \gamma_m}{\partial X}\gamma_i dXdY + A(\varphi)\frac{2Pr}{\varepsilon}\sum_{m=1}^{N} U_m\int\frac{\partial \gamma_m}{\partial X}\frac{\partial \gamma_i}{\partial X}dXdY$$
$$+A(\varphi)\frac{Pr}{\varepsilon}\sum_{m=1}^{N} U_m\int\left[\frac{\partial \gamma_m}{\partial Y}\frac{\partial \gamma_i}{\partial Y}\right]dXdY + A(\varphi)\frac{Pr}{\varepsilon}\sum_{m=1}^{N} V_m\int\frac{\partial \gamma_m}{\partial X}\frac{\partial \gamma_i}{\partial Y}dXdY$$
$$-A(\varphi)\frac{Pr}{Da}\int\left(\sum_{m=1}^{N} U_m\gamma_m\right)\gamma_i dXdY - S(\theta)\int\left(\sum_{m=1}^{N} U_m\gamma_m\right)\gamma_i dXdY \quad (24)$$

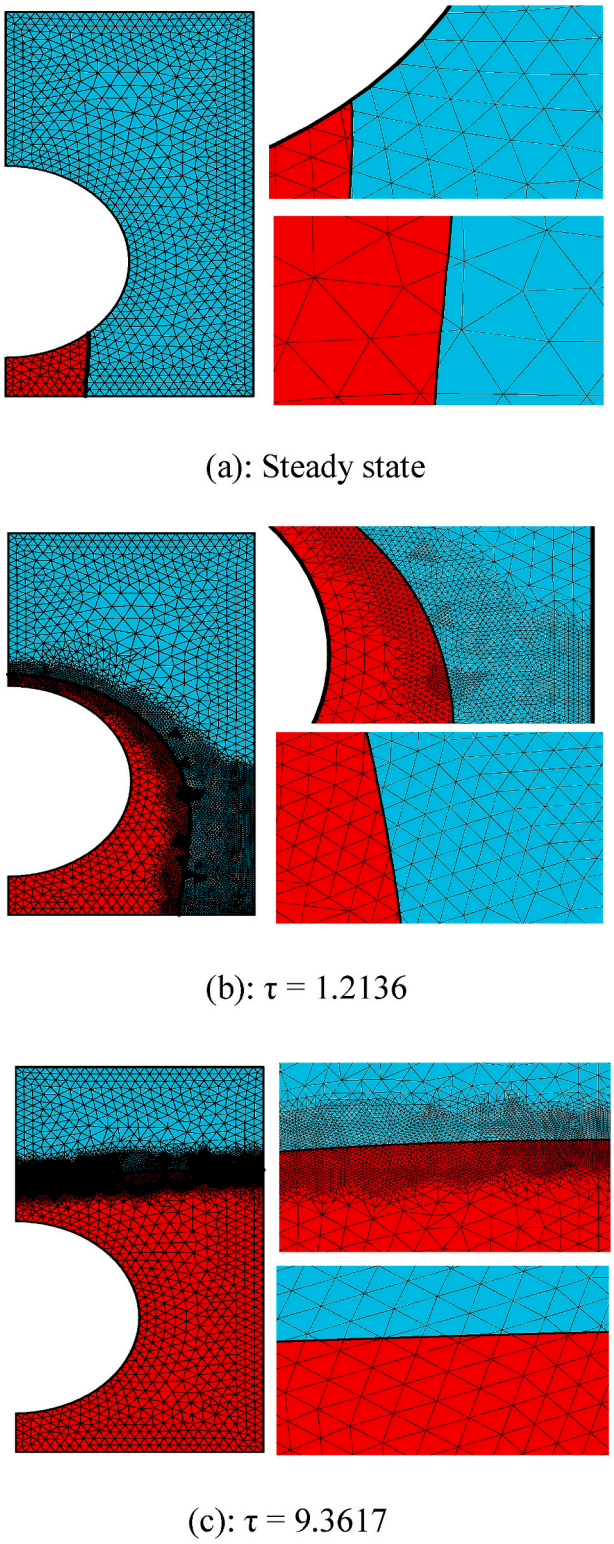

Fig. 4. Display of the deformable mesh (Case IV) during the melting process.

copper metal-foam and saturated with the paraffin wax is considered as a case study here. The 5PPI copper metal-foam has a porosity value of $\varepsilon = 0.975$ and permeability equal to 2.7×10^{-7} m^2, according to Refs. [51]. The fusion temperature of the paraffin wax is $T_f = 50$ °C, and the effective thermal conductivity of copper foam and paraffin wax is reported as $k_m = 4.8$ W/m.K [38]. The top wall is assumed to be at the

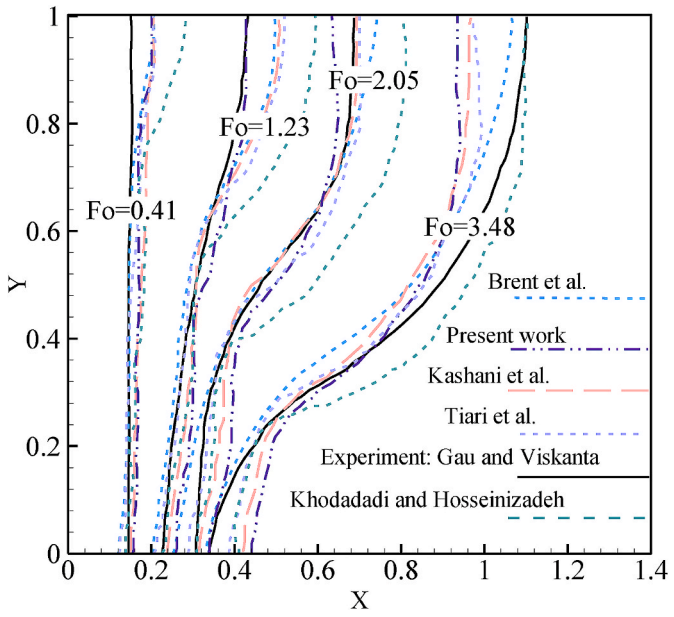

Fig. 5. A comparison between the present study and the literature results Tiari et al. [58], Khodadadi et al. [59], Kashani et al. [60] and Brent et al. [61].

uniform temperature of $T_\infty = 14$ °C, and the heat flux of the circular shell is $q = 400$ W/m^2.

The employed thermophysical properties for the utilized materials are summarized in Table 2. According to the heat flux model explained earlier, $\gamma = 3$ assumed for the case study with a pulse duration of 1200 s started at 200 s, and ended at 1500 s. The calculated non-dimensional parameters are $Ra = 88693$, $Da = 1.9937 \times 10^{-4}$, $Pr = 1.5334$, $\varepsilon = 0.975$, $\theta_f = 11.739$, $(\rho C_p)_{m,s}/(\rho C_p)_{m,l} = 1$, $k_{m,s}/k_{m,l} = 1$, $\gamma = 3$, $\tau_1 = 0.346$, $Bi = 0.153$, and $\delta\tau = 2.0804$. These mentioned values of the non-dimensional parameters will be used for the results of this study, apart from that will be stated.

2. Validation and grid check

A mesh study is performed to ensure the accuracy of the results and mesh quality by utilizing the non-dimensional parameters expressed in sub-section 3.2. Six different grid sizes are utilized for grid independency-check. The results for the average battery shell temperature ($\theta_{b,ave}$) and melting volume fraction (*MVF*) are listed in Table 3 for different cases.

Fig. 2 and Fig. 3 show grid independence for $\theta_{b,ave}$, and *MVF* for Cases II to V. It can be concluded that the results for Case IV and Case V are almost equivalent, while the other two Cases experience more error. By considering that the computational cost increases extensively by increasing the grid size, Case IV is chosen as the optimum grid size for the present study.

The deformable grid patterns for Case IV are illustrated in Fig. 4, during the melting process for time-independent and time-dependent solutions. Fig. 4 (a) demonstrates the employed mesh at the beginning of the analysis. For capturing the velocity and temperature gradient close to the walls, it can be seen that the mesh has a smaller size in these regions. Mesh structure at non-dimensional times $\tau = 1.2136$ and $\tau = 9.3617$ are also shown in Fig. 4(b) and (c). For accuracy of the results in the phase change region, mesh adopts a much finer size near the melting front, five times smaller than the regular areas. According to Fig. 4(b) and (C), the liquid-solid interface (fusion region) moves over time, so the grid size is chosen as extremely fine elements by advancing of the melting process beyond the hot circular shell.

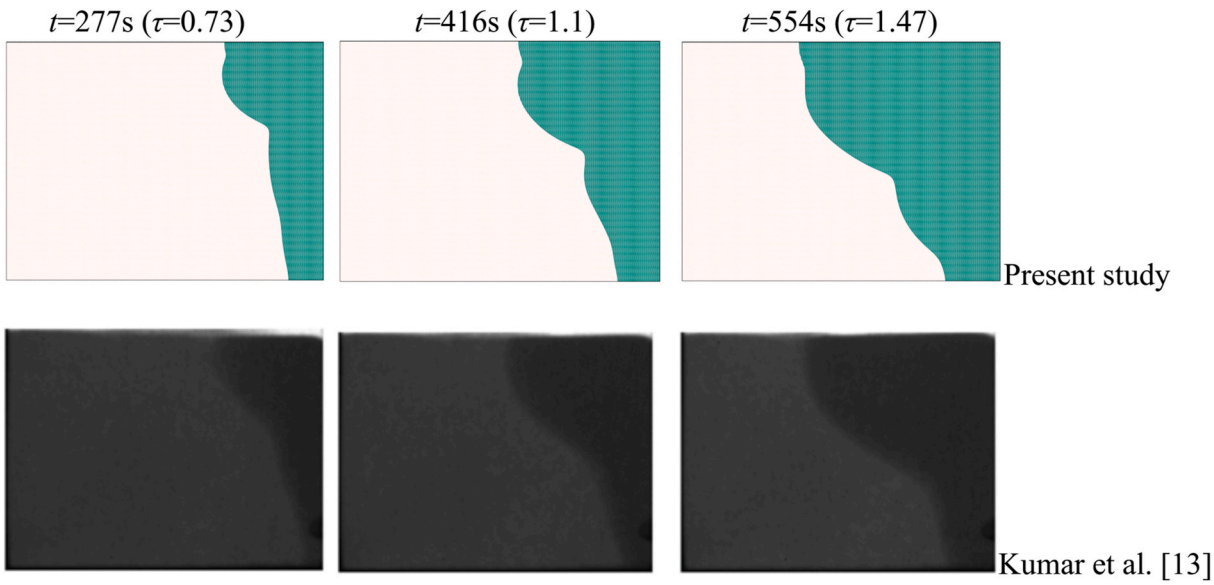

Fig. 6. Melting images obtained by the experiments of Kumar et al. [13] and the present results at three different non-dimensional time steps.

2.1. Validation

In this section, different comparisons are conducted between the results of the present study with some of the theoretical and experimental results available in the literature to confirm the accuracy and precision of the introduced model of phase change and the computations expressed in the present study. For the first case, the experimental results of Gau and Viskanta [59] and the numerical studies available in the literature [60–63] for melting of pure gallium in a rectangular cavity with high/width ratio of 0.714. The assumptions considered for this case are as: $\varepsilon = 1$, $Da \rightarrow \infty$, the left wall of the cavity is at a constant temperature, and the other walls are adiabatic. For having a credible assessment, the results are compared when $Pr = 0.0216$, $Ra = 6 \times 10^{+5}$, and $Ste = 0.039$. The melting fronts for $\tau = 0.41$, 1.23, 2.05, and 3.48 are plotted in Fig. 5. A superb agreement can be seen in the trend of numerical results, and also the numerical results of the present study agree with the experimental results.

Kumar et al. [13] addressed the melting of lead in a cavity using the thermal neutron radiography technique. Hence, this work is chosen as the second case study for comparing with the present study. The right wall of the test set-up cavity filled with the lead was subjected to uniform heat flux while the rest of the cavity walls was adiabatic. Fig. 6 illustrates the melting images obtained in Ref. [13] by and the present results at three different non-dimensional time steps. Both studies are

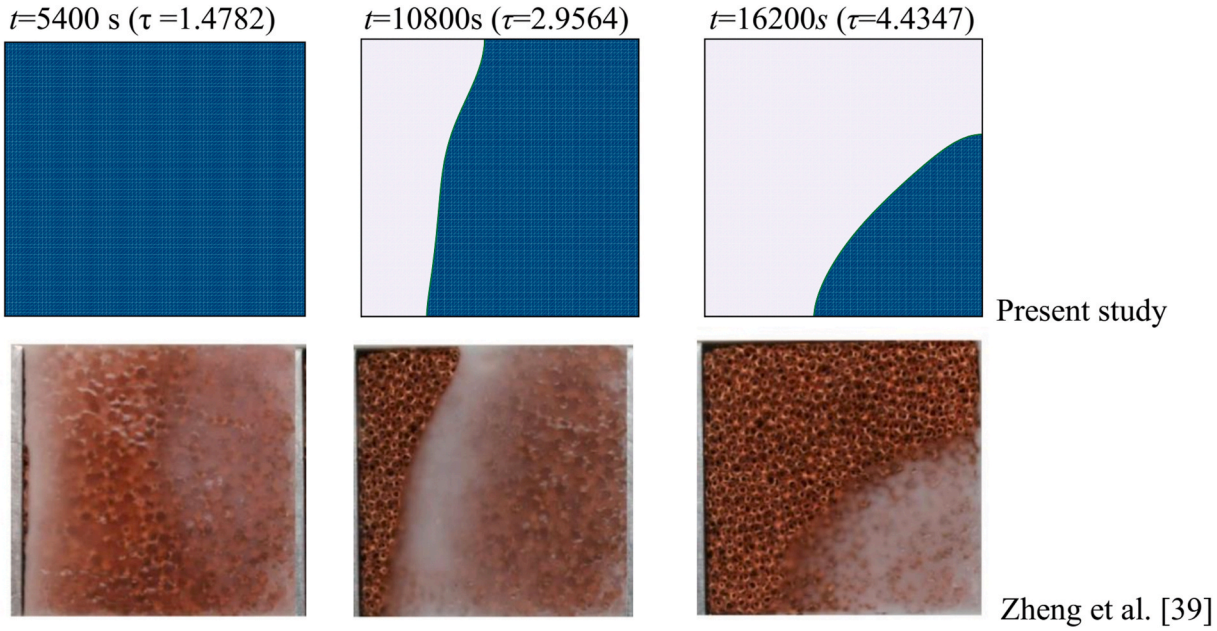

Fig. 7. A comparison between the numerical results of the current work and experimental results of Zheng et al. [39].

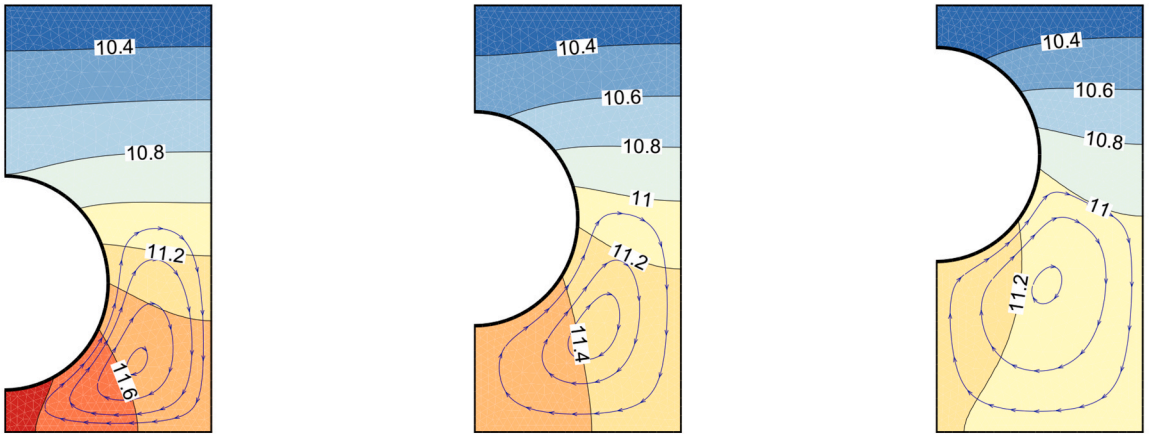

(a): $\theta_{b,ave}$=11.337, *MVF*=0.48 (b): $\theta_{b,ave}$=11.086, *MVF*=0.56 (c): $\theta_{b,ave}$=10.852, *MVF*=0.66

E_C= -0.15, *Ra*=17592 E_C=*0*, *Ra*=17592 E_C=*0.15*, *Ra*=17592

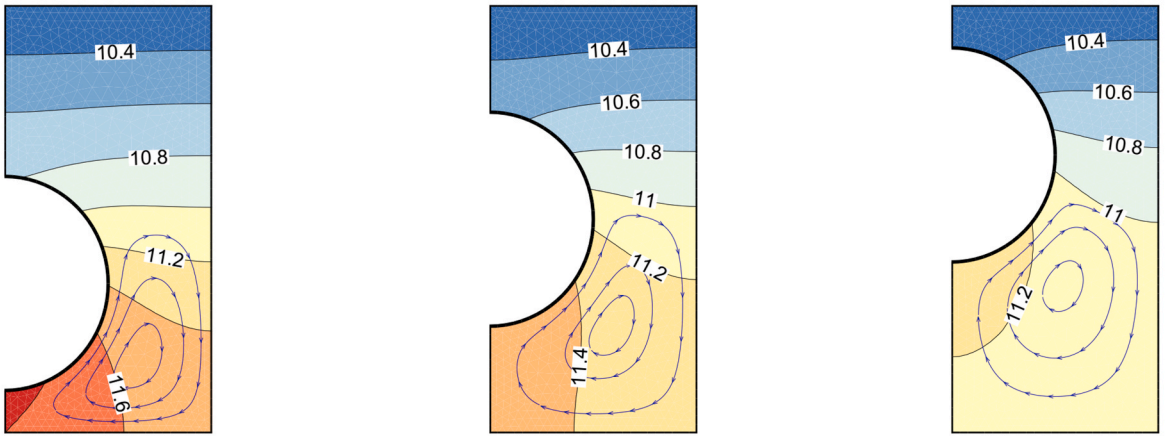

(d): $\theta_{b,ave}$=11.322, MVF=0.47 (e): $\theta_{b,ave}$=11.071, MVF=0.56 (f): $\theta_{b,ave}$=10.843, *MVF*=0.66

E_C= *-0.15*, *Ra*=95345 E_C=0, *Ra*=95345 E_C=0.15, *Ra*=95345

Fig. 8. Temperature contours and streamlines (in the same figure) for the default case ($Da = 1.993 \times 10^{-4}$, $Pr = 1.533$, $\varepsilon = 0.975$, and $\gamma = 0$), and different values of E_C number.

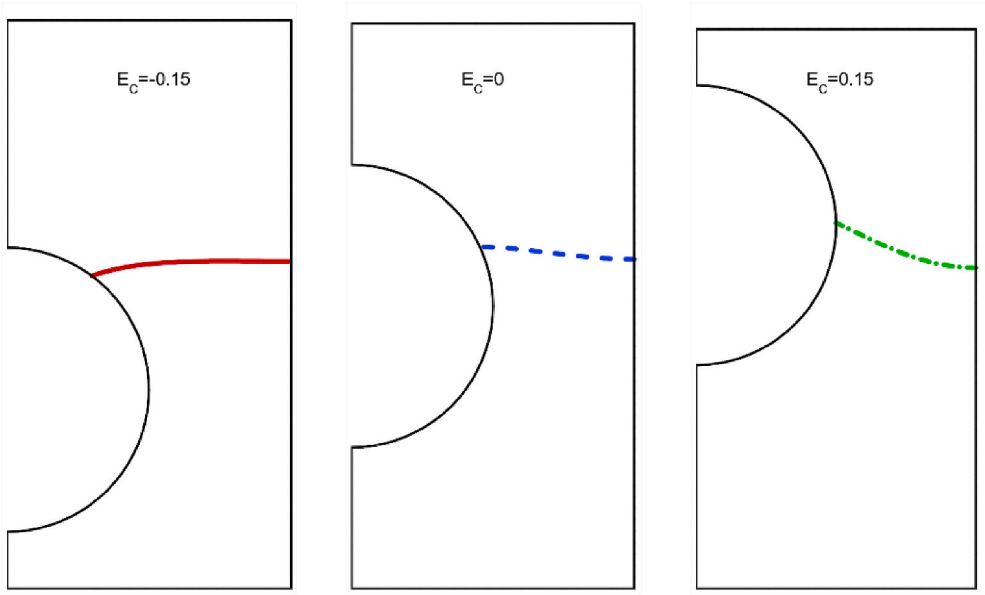

Fig. 9. Displacement of fusion interface ($\varphi = 0.5$) from various values of E_C.

performed with the following conditions: $Ste = 0.4$, $Pr = 0.0236$, $Ra = 1.4 \times 10^{+7}$ and the heater input equal to16.3 kW/m^2.

In the steady-state condition and by overlooking the conjugate effect, the problem changes to a regular porous medium saturated with a pure fluid. This case has been analyzed by several investigators. In the case of $Ra \times Da = 100$, the Nusselt number was reported as 3.113 [64], 3.160 [65], 3.104 [33], and it was found as 3.111 in the present study.

For validating the results for the melting of paraffin-copper foam in a cavity, experimental study of Zheng et al. [39] is adopted to compare with the present study (Fig. 7). The porosity of the porous medium is reported as $\varepsilon = 0.95$ with a pore size of 5PPI. The thermophysical properties for paraffin wax and copper foam are listed in Table 1. As described in the experimental work of Xiao et al. [38] for a cavity with a size of $H = 0.1$ m, the effective thermal-conductivity was $k_{eff} = 5$ W/m.K, while the hot (left) wall was subject to a constant heat flux of $q''_0 = 1150$ W/m^2. The melting interfaces of these two studies are in good agreement in all the three-time steps.

3. Results and discussion

The numerical results for the heat transfer of the phase change heatsink are presented for two cases. The first case is when the heatsink is in a steady-state ($\gamma = 0$) situation, and there is an energy balance between the power of heat flux and the heat transfer to the external space. The unsteady heat transfer of the phase change heatsink is the second case and occurs when the enclosure is subjected to a heat pulse.

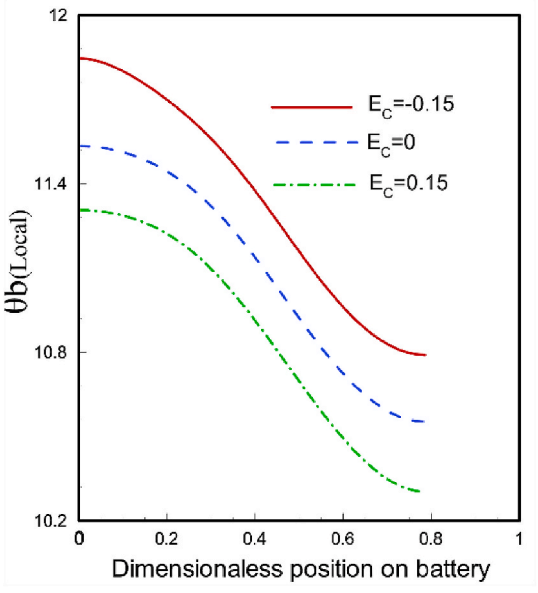

Fig. 10. The local temperature of battery shell, θ_b, for various values of E_C.

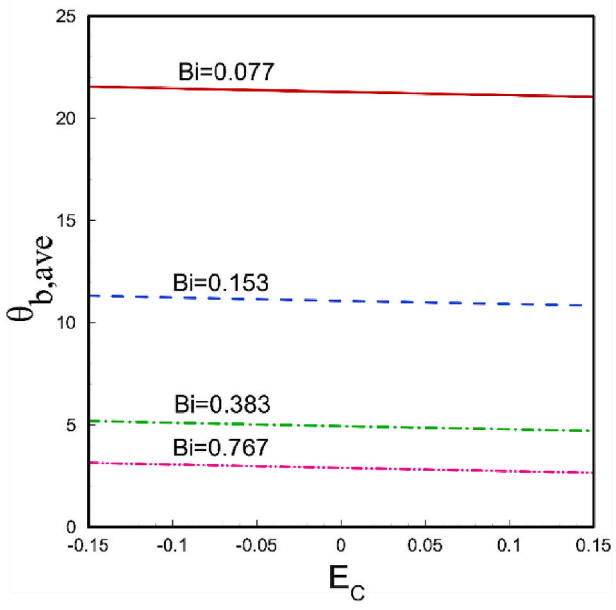

Fig. 11. $\theta_{b,ave}$ as a function of E_C number for different Biot numbers.

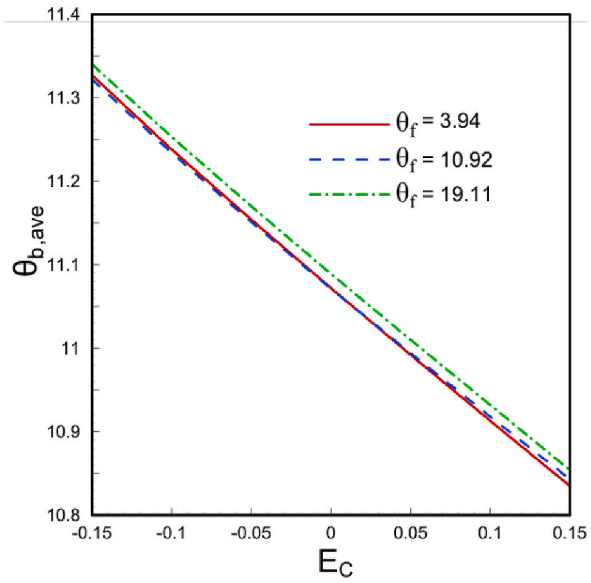

Fig. 12. $\theta_{b,ave}$ as a function of E_C number in different fusion temperatures.

In the steady-state situation, based on the external cooling load, the heatsink can be in a liquid, solid or solid/liquid state. The existence of an active heat pulse increases the heat flux power of the battery in the unsteady case and will result in a transient heat transfer phenomenon. The non-dimensional parameters introduced in the early sections of this study are adopted for both steady and unsteady analysis.

3.1. The steady-state heatsink with $\gamma = 0$

In Fig. 8, steady-state streamlines, isotherm patterns, and melting front surface of the heatsink are depicted for different values of the E_C and Ra numbers. As stated before, E_C number indicates the vertical position of the battery in the cavity. In the steady-state situation, $\gamma = 0$ and the battery produce a constant thermal power which results in a thermally balanced condition in the system. The produced thermal energy of the battery spreads into the molten area and then reaches the solid region. The heat moves toward the top cold free stream and will be released from the battery pack.

Streamlines in Fig. 8 indicates the liquid region, which means no streamline exists in the solid area. The average temperature of the battery-shell (hot element) and normal melt volume fraction (MVF) are also informed below each contour. It can be concluded that by increasing the E_C number, natural convection becomes the dominant heat transfer mechanism, and consequently, a reduction in the temperature of the hot wall (shell) occurs. Comparing the contours in Fig. 8 indicates that increasing the Rayleigh number has no significant influence on the streamlines, while it causes a slight reduction in the temperature contours on the left side of the heatsink. Results for $Ra = 17592$ show that increasing the E_C number reduces the dimensionless average temperature of the battery shell (hot wall) from 11.337 to 10.852 and increases the value of the melting volume fraction from 0.48 to 0.66. A similar trend also occurred for $Ra = 95345$. Variation of MVF indicates that thermal diffusivity or conduction has a minimal effect on the heat transfer inside the heatsink.

Fig. 9 illustrates the position of the fusion interface for three different values of E_C number ($E_C = -0.15$, 0, and 0.15) in the steady-state situation. As stated before, $\varphi = 0.5$ is considered as the fusion interface's position. It can be seen that by raising the hot element's position in the heatsink, the melting front elevates slightly, resulting in higher PCM melting in the cavity.

Fig. 10 depicts the local temperature of the battery shell, $\theta_{b,local}$, as a function of dimensionless position on the battery for different values of E_C numbers. The local temperature decreases for all three cases by moving along the hot element from the bottom to the top. It can be seen in Fig. 10 that by decreasing the E_C number, the shell experiences a lower temperature at different locations of the shell. This is since moving the shell upward decreases the overall distance between the cold surface and consequently reduces the thermal resistance.

Fig. 11 shows the changes in the average temperature of the battery

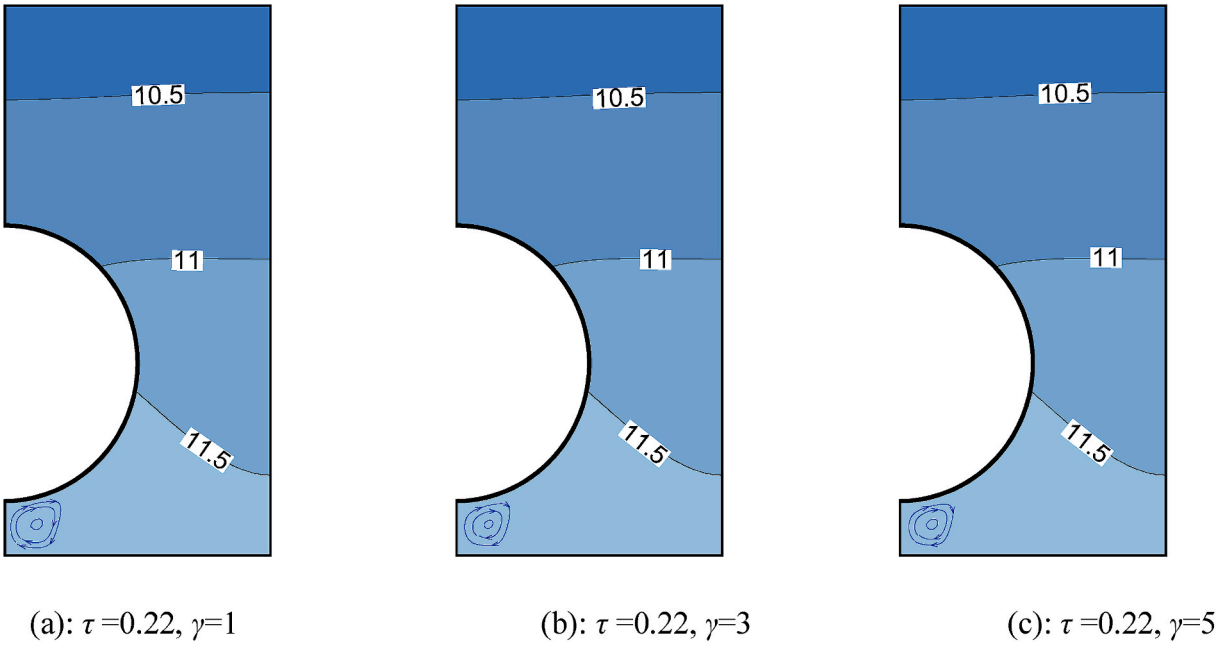

Fig. 13. The effect of intensity of the active heat flux (γ) on the phase change behavior of the heatsink.

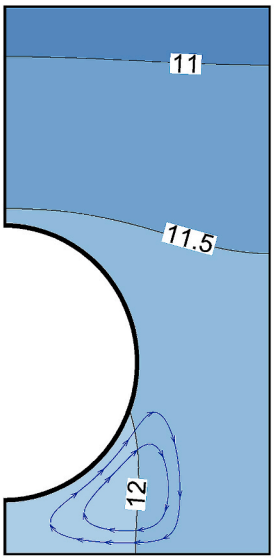

(d): τ =2.6, γ=1

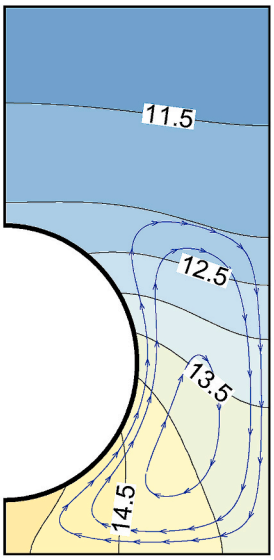

(e): τ =2.6, γ=3

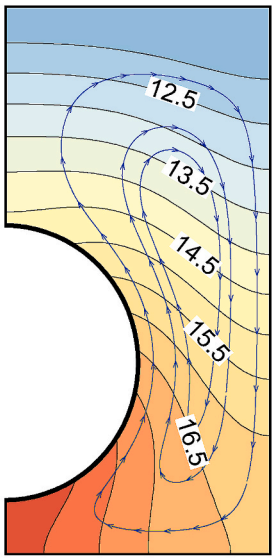

(f): τ =2.6, γ=5

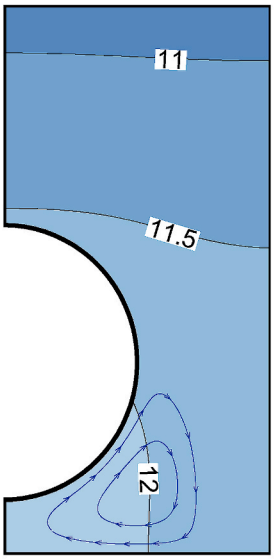

(g): τ =2.95, γ=1

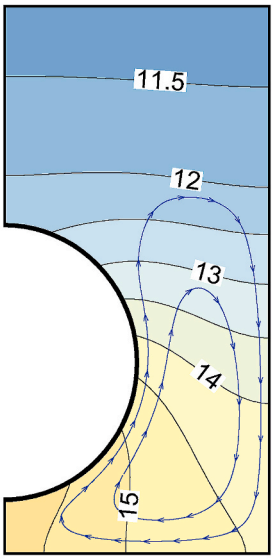

(h): τ =2.95, γ=3

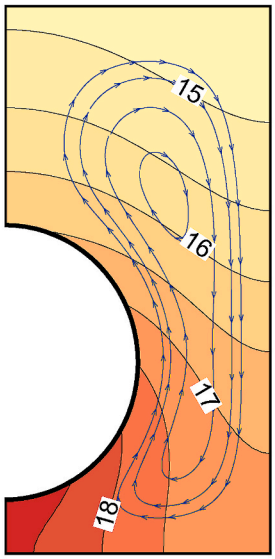

(i): τ =2.95, γ=5

Fig. 13. (*continued*).

shell for different values of the Biot number (external cooling power) as a function of the E_C number. The values of $\theta_{b,ave}$ decreases minimally and linearly by increasing the E_C number. The Biot number has a significant effect on the average battery shell temperature. As an example, a decrease in The Biot number from 0.383 to 0.077 resulted in about 4.4 times growth of $\theta_{b,ave}$.

The variation of the average battery shell temperature as a function of the E_C number is illustrated in Fig. 12 for different dimensionless fusion temperatures (θ_f). Increase of fusion temperature results in a rise in the portion of the solid region inside the heatsink. By considering that natural convection in the solid region of the PCM vanishes, thermal resistance increases significantly in this region in comparison with the molten region. Accordingly, any expansion of the solid PCM regions will elevate the element temperature. Fig. 12 shows that by increasing the E_C number, the average battery shell temperature declines linearly and gradually. Also, $\theta_{b,ave}$ does not change significantly in a wide range of dimensionless fusion temperatures. For the mentioned values of the θ_f in Fig. 12, $\theta_{b,ave}$ experienced less than 4.5% reduction for $-0.15<E_C<0.15$.

3.2. The unsteady heat transfers due to a heat pulse

In this section, for studying the unsteady behavior of the battery for three different pulse powers, the E_C number is selected as -0.15. The streamlines and isotherm contours are plotted in Fig. 13 for $\gamma = 1, 3, 5$ in various dimensionless time steps. As it is illustrated in Fig. 13(a)–(c), the streamlines and isotherms are remained constant for different values of γ *at* $\tau = 0.22$, since these results are for the initial solution before

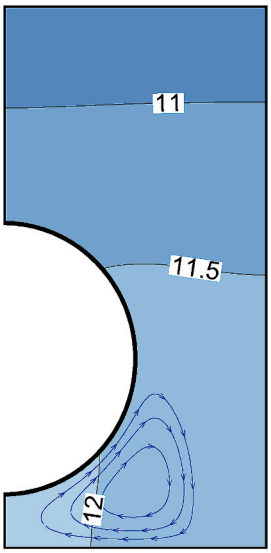

(k): τ =3.29, γ=1

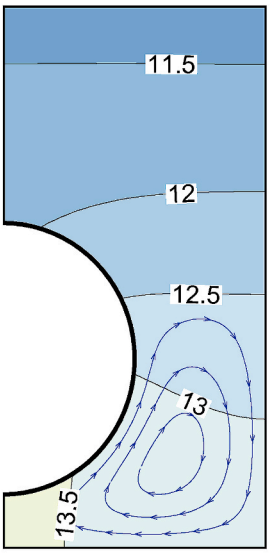

(l): τ =3.29, γ=3

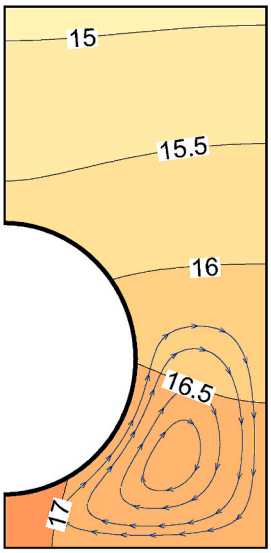

(m): τ =3.29, γ=5

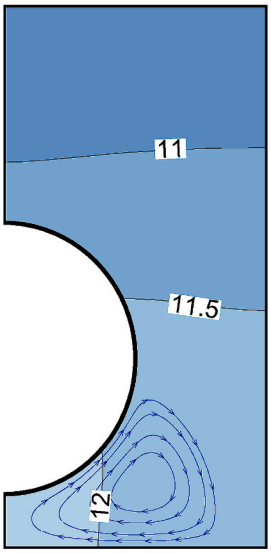

(n): τ =4.33, γ=1

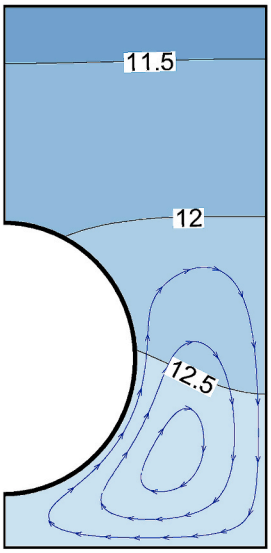

(o): τ =4.33, γ=3

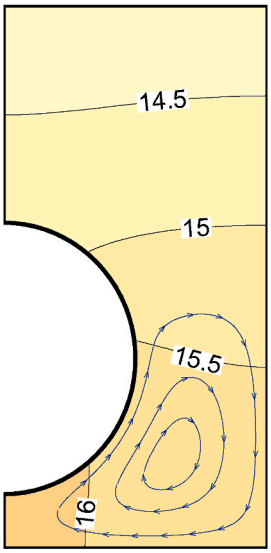

(p): τ =4.33, γ=5

Fig. 13. (*continued*).

activation of the heat pulses at $\tau = 0.347$.

The streamlines and isotherms for time step $\tau = 2.6$ are depicted in Fig. 13(d)–(f) for pulse powers with $\gamma = 1, 3, 5$, respectively. Since the heat pulse deactivates at $\tau = 2.6$, Fig. 13(d)–(f) illustrate the results quite after the heat pulse is turned off. It can be seen in Fig. 13(f) that almost the whole enclosure is filled with the molten PCM for the case of $\gamma = 5$. Here the contour level of $\theta = 12$ can be considered as the fusion temperature and the melting front in the heatsink. Streamline distribution in these figures indicates that for the low heat pulse case ($\gamma = 1$), only a small region under the heater is melted, and the rest of the heatsink is covered by the solid PCM.

As the heat pulse increases for the case of $\gamma = 3$, the molten area expands and fills about half of the heatsink. Streamlines are well distributing by boosting heat power. In the case of $\gamma = 5$, the molten area develops almost the whole enclosure. It can be observed in Fig. 13(f) that the raise of pulse power increases the temperature near the battery shell and strengthen the temperature gradient in this region.

Streamlines and isotherms for $\gamma = 1, 3, 5$ are illustrated in Fig. 13(g), (h) and (i) at dimensionless time $\tau = 2.95$. It is a short time after that the heat pulse is deactivated, and the heat flux is resumed to the steady condition. The results for $\gamma = 1$ at $\tau = 2.6$ and $\tau = 2.95$ are almost similar, and no significant changes can be noticed in this period. Although the heat pulse is previously turned off, the time was not long enough to witness the propagation of its effects. The streamlines expanded slightly toward the top in the case of $\gamma = 3$. A comparison between Fig. 13(f) and (i) reveals a significant change in the streamlines and isotherms in this period of the time for the case of $\gamma = 5$. This is since after the transient heat pulse was terminated, the induced heat was still

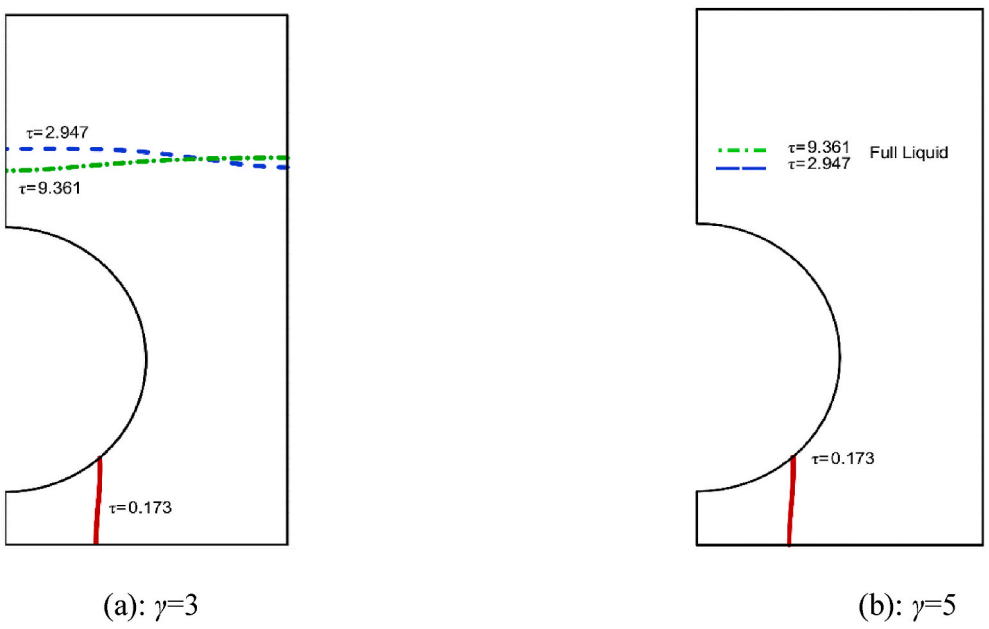

Fig. 14. The displacement of the melting front ($\varphi = 0.5$) over time.

spreading toward the top region of the enclosure. This occurs due to the extreme power of the heat pulse applying to the PCM.

Fig. 13(k)-(m) shows the result for $\tau = 3.29$ which is for $\Delta\tau = 0.69$ after the heat pulse was turned off. The result for $\gamma = 1$ shows denser streamlines on the left bottom of the enclosure in comparison with the previous time step. The temperature at the top region of the heatsink also tends to decrease due to the existence of the external cooling mechanism on the top wall. In the case of $\gamma = 3$, streamlines show a smaller molten region at the bottom half of the enclosure. The temperatures experienced a moderate reduction in this time step. Comparing Fig. 13(i) and (m) confirms the existence of the same trend for the case of high pulse power $\gamma = 5$. Indeed, the molten PCM is limited to the bottom half of the heatsink and the temperature drops significantly in the entire heatsink especially below the hot element.

Fig. 13(n), (o) and (p) illustrate the isotherm and streamlines for low ($\gamma = 1$), moderate ($\gamma = 3$) and intense ($\gamma = 5$) heat pulse at $\tau = 4.33$. The streamlines of these figures are similar, while the temperature distributions are different due to the difference in the power of heat pulse applied to the element. By considering that the bottom wall is adiabatic while the top wall is connected to external cooling support, the solidification starts from the top region of the heatsink.

Fig. 14 displays the fusion interface behavior for moderate ($\gamma = 3$)

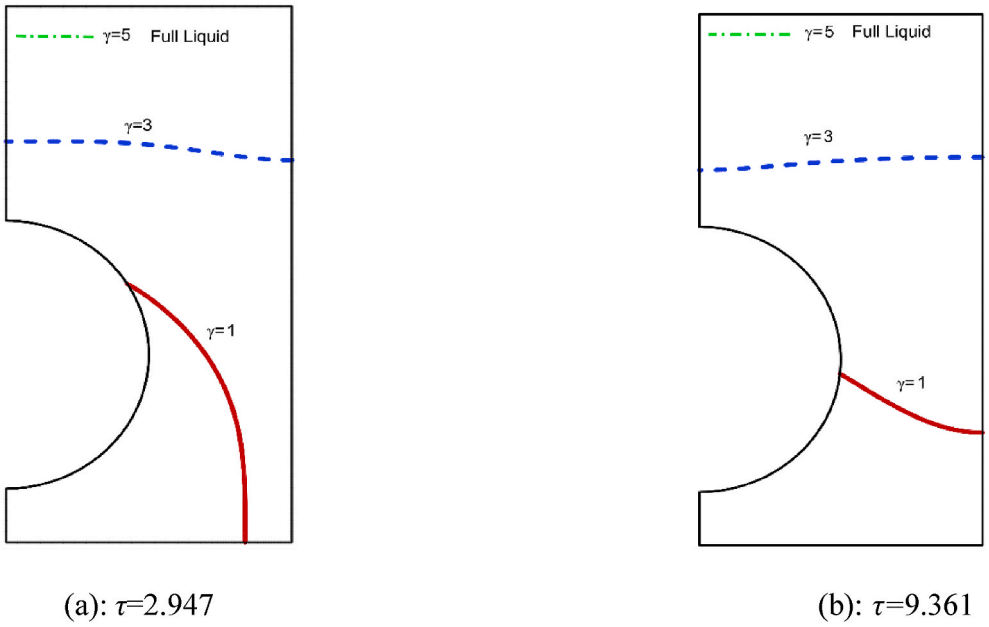

Fig. 15. The behavior of the fusion interface ($\varphi = 0.5$) for various heat flux at different times.

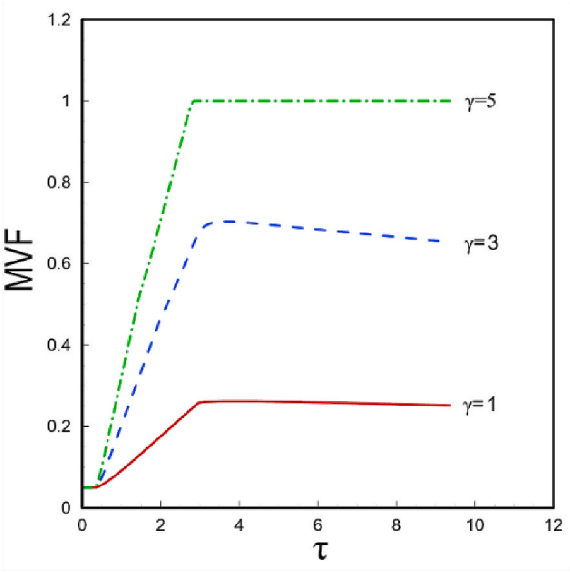

Fig. 16. Melt volume fraction during time for various values of γ

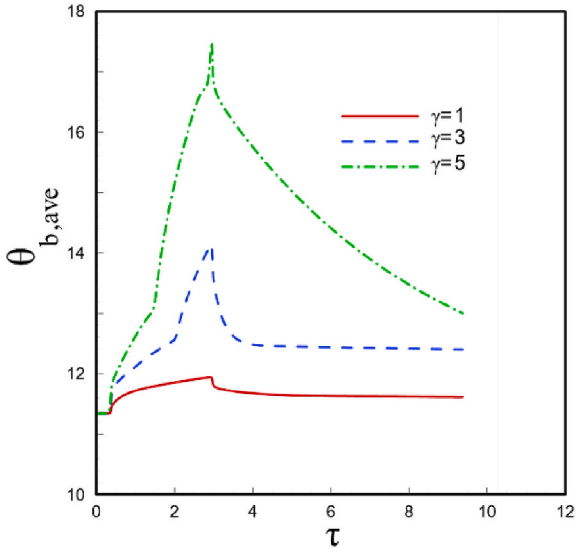

Fig. 17. $\theta_{b,ave}$ during the time for various values of γ.

and intense ($\gamma = 5$) heat flux at different time steps. As stated before, the melting front is when the melt volume fraction, φ, *is* equal to 0.5. It can be seen in Fig. 14 that at $\tau = 0.173$ the fusion interfaces for both cases are similar, the reason is that the enclosure is at the steady condition before the initiation of the heat pulse. In Fig. 14. (a), at $\tau = 2.947$, the melting develops toward the top region of the heatsink while the solidification ($\tau = 9.361$) occurs at a lower position close to the hot element and higher at the right side of the heatsink. For the case of intense heat flux, the PCM is entirely in the liquid state at both time steps. A much higher time is required to compensate for the high value of the absorbed thermal energy and return to the steady condition.

The behavior of the fusion interface for various heat flux is plotted in Fig. 15(a) and (b) for two different time steps ($\tau = 2.947$ and $\tau = 9.361$). As was shown in Fig. 14, the fusion interface is placed far away from the battery shell in higher values of γ. For $\gamma = 5$, the hot liquid PCM has filled the entire heatsink at both dimensionless times. While for $\gamma = 3$ the liquid region changed slightly in this period of the time, the changes $\gamma = 1$ is more noticeable. At $\tau = 2.947$, the molten region was closer to the hot element creating a thick layer of the solid PCM near the right wall. After $\Delta\tau = 6.414$, the melting front advanced toward the bottom wall and shifted to the right side covering the entire bottom region of the enclosure with liquid.

Fig. 16 shows the variation of the melting volume fraction as a function of non-dimensional time for different values of heat pulse. Due to the initial steady condition, MVF has a constant value for different heat pulse powers. After activation of the heat pulse, the melting volume fraction increases sharply until reaching a maximum value. The degree of growth is higher for higher values of γ. As stated before and can be seen in Fig. 16., the rise of *MVF* continues after the heat pulse turns off. In the case of intense heat pulse, $\gamma = 5$, *MVF* reaches and remains in its maximum possible value ($MVF = 1$) due to the fact that PCM is fully in the liquid state. After reaching the maximum value of *MVF* for the case of moderate heat pulse, the solidification phenomenon starts slightly, and the *MVF* value decreases gradually.

Fig. 17 illustrates the changes in the average dimensionless temperature of the battery shell during the non-dimensional time for different magnitudes of heat pulse. After activation of the heat pulse, $\theta_{b,ave}$ experiences a dramatic increase for $\gamma = 3$ and $\gamma = 5$ until reaching a maximum. Unlike the variation of MVF, $\theta_{b,ave}$ drops significantly after the heat pulse turns off. This reduction for $\gamma = 5$ takes a long time because the temperature difference is too high, and it needs more time to return. The change of the average dimensionless temperature for $\gamma = 1$ is not as notable as its variation for higher heat pulse powers.

Fig. 18 shows the impact of γ and Rayleigh and Darcy in the term of Rayleigh-Darcy (RD) dimensionless number on the average dimensionless temperature of the battery shell at a specific time duration. As seen, the average wall temperature increases when γ changes from 1 to 5. This observation is in agreement with the outcomes of Fig. 17. In the case of weak heat pulse ($\gamma = 1$), the variation RD does not change the thermal behavior of the wall, as depicted in Fig. 18(a). However, as the heat pulse power rises, this pattern changes. Fig. 18 (b) and (c) are plotted for the cases of $\gamma = 3$ and $\gamma = 5$. As seen, an increase in *RD* number reduces the average temperature of the wall.

This phenomenon is attributed to the effect of heat flux on the melting process and natural heat transfer convection. The presence of an active pulse boosts the heat flux, and therefor, the wall temperature growth. Consequently, the extra energy of the hot wall improves the melting process and expands the liquid area. The better convection heat transfer leads to a better cooling power and a lower wall temperature. Thus, when the RD raises, the velocity of liquid circulation increases, which leads to the enhancement of heat transfer convection coefficient.

In the case of small RD numbers, the increase of wall temperature is quite notable ($RD = 10$), since the heat transfer mechanism is conduction dominant. In contrast, the increase of *RD* ($RD > 100$) leads to a convection dominant heat transfer mechanism, and as soon as a strong convection heat transfer commences in the heatsink, a further increase of *RD* does not change the wall temperature behavior.

The changes in the heatsink efficiency before and after activation of the heat pulse is displayed in Fig. 19. By applying the heat pulse, the efficiency increases suddenly, about seven times for $\gamma = 5$. The higher the heat pulse power, the higher the reduction of heatsink efficiency during the heat pulse activation. With a small delay after the end of the heat pulse, the efficiency drops dramatically, even less than the steady-state condition, and after a long period, it will reach the initial

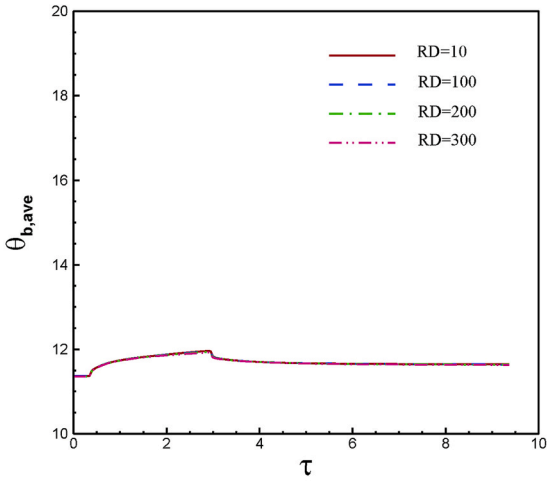

(a): $\gamma = 1$

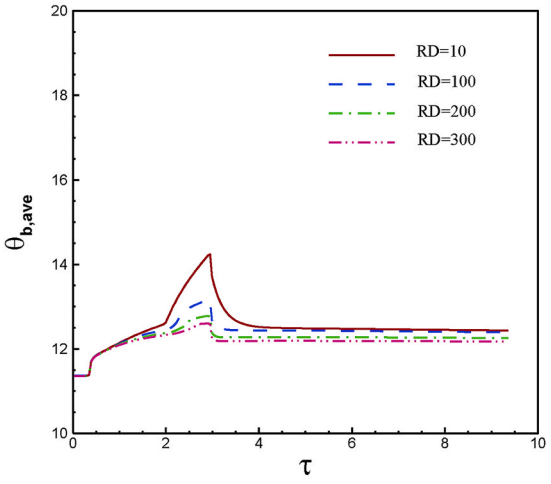

(b): $\gamma = 3$

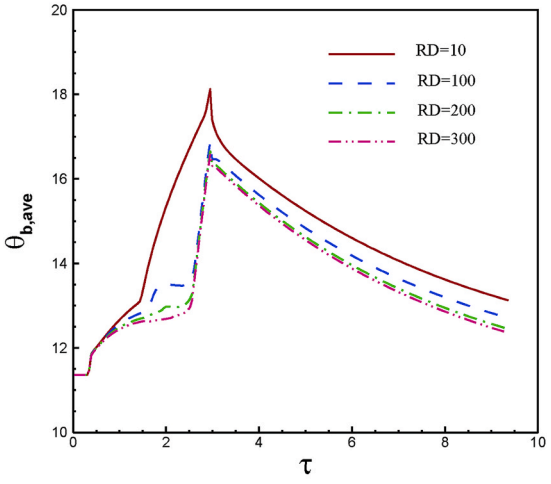

(c): $\gamma = 5$

Fig. 18. The dimensionless average wall-temperature ($\theta_{b,ave}$) over time for various values of *RD* when $Da = 1.994 \times 10^{-4}$.

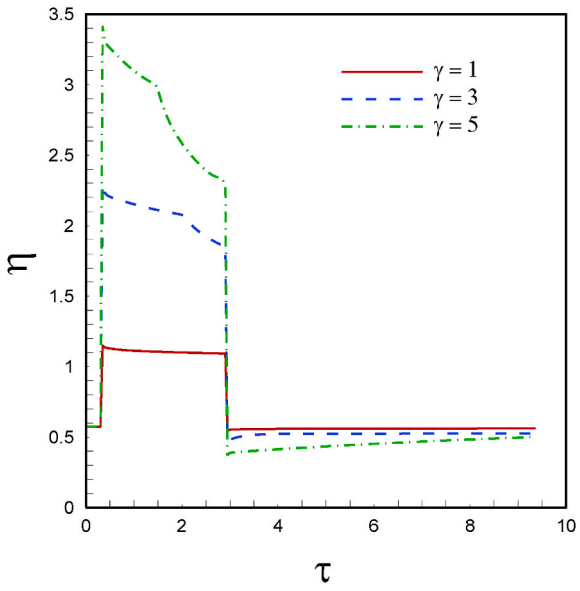

Fig. 19. Heatsink efficiency variation for various values of γ.

efficiency. The natural convection and conduction heat transfers play significant roles in the PCM/copper foam heatsink. Indeed, the majority of the heat is transferred by conduction mechanism, especially in deeper parts. The liquid phase region develops by increasing the γ and the average temperature of the battery shell declines to improve the heat transfer to the ambient environment. In contrast, η face a reduction in pulse duration. When heat pulse is applied to the system, $\theta_{b,ave}$ increases significantly, which leads to the reduction of η at constants values of γ.

4. Conclusion

Heat transfer and thermal behavior of a battery cell filled with PCMs embedded in metal-foam for different values of heat pulse were theoretically investigated in this paper. The studied heatsink was included of a semi-circular battery cell, which was considered as the thermal source with unsteady a heat pulse power. The left and right walls of the enclosure had the symmetry boundary condition while the bottom wall was adiabatic, and the top wall was subjected to external convection cooling. By using dimensionless variables, the presented governing equations for heat transfer and phase change flow plus the boundary conditions were transformed into non-dimensional forms. These equations are solved by using the finite element method with grid adaptation and automatic time step schemes. The local thermal equilibrium model was assumed between the PCM and metal foam, and hence, the outcomes are limited to metal foams with high pore densities. At first, the steady-state behavior of the heatsink was presented for various locations of the battery cell. Then the isotherms and streamlines for unsteady cases with three different heat pulse powers were addressed in different time steps. The following conclusions can be made based on the results:

1 grid adaption helped to achieve accurate results, which were in an excellent agreement with the experimental and numerical studies in the literature.
2 In the steady-state condition, as the battery cell approaches the cold top wall, the melt volume fraction increases inside the heatsink, and the thermal distribution becomes more uniform, especially at the bottom of the heatsink.
3 In the condition with no heat pulse, by decreasing the Biot number, the average temperature of the semicircular shell wall experienced significant growth.
4 By increasing the heat pulse power, the molten region in the heatsink grows and moves toward the top wall. At high heat pulse, the molten PCM was expanded in the entire enclosure while for lower heat pulse powers, the top part of the heatsink was still in the solid condition.
5 By applying a high heat pulse, the average temperature of the battery cell increases sharply, and the increase in PCM temperature also continues for a while after the heat pulse was terminated. It occurs due to the extreme magnitude of the heat pulse, which needs time to travel inside the PCM even after turning off the heat pulse.
6 The battery heatsink efficiency was higher than unity for all the unsteady cases. By activation of the heat pulse, the efficiency increases sharply. The results revealed that by increasing the magnitudes of the heat pulse, the efficiency also increases.
7 The increase of Rayleigh-Darcy number boost the convection mechanis. In the low values of Rayleigh-Darcy number, the heat transfer mechanis is mostly conduction dominant, and the presence of a strong pulse power increases the wall-temperature significantly. An stablished convection dominant regime (high Rayleigh-Darcy number) could reduce wall temperature in the presence of a strong heat pulse. However, a further increase of Rayleigh-Darcy number induces minimal changes on the wall temperature when there is a strong convection flow.

Declaration of competing interest

The authors clarify that there is no conflict of interest for report.

Appendix A. Supplementary data

Supplementary data to this article can be found online at https://doi.org/10.1016/j.ijthermalsci.2020.106514.

References

[1] N. Zhang, Y. Yuan, X. Cao, Y. Du, Z. Zhang, Y. Gui, Latent heat thermal energy storage systems with solid–liquid phase change materials: a review, Adv. Eng. Mater. 20 (2018) 1700753.
[2] X. Jin, S. Zhang, X. Xu, X. Zhang, Effects of PCM state on its phase change performance and the thermal performance of building walls, Build. Environ. 81 (2014) 334–339.
[3] C. Zhang, Y. Chen, L. Wu, M. Shi, Thermal response of brick wall filled with phase change materials (PCM) under fluctuating outdoor temperatures, Energy Build. 43 (2011) 3514–3520.
[4] A. Athienitis, Y. Chen, The effect of solar radiation on dynamic thermal performance of floor heating systems, Sol. Energy 69 (2000) 229–237.
[5] D. Buddhi, Thermal performance of a shell and tube PCM storage heat exchanger for industrial waste heat recovery. Proc. ISES Solar World Congress, 1997.
[6] A. Andreozzi, B. Buonomo, D. Ercole, O. Manca, Solar energy latent thermal storage by phase change materials (PCMs) in a honeycomb system, Therm. Sci. Eng. Progr. 6 (2018) 410–420.
[7] S. Shi, Y. Xie, M. Li, Y. Yuan, J. Yu, H. Wu, B. Liu, N. Liu, Non-steady experimental investigation on an integrated thermal management system for power battery with phase change materials, Energy Convers. Manag. 138 (2017) 84–96.
[8] Y.-C. Weng, H.-P. Cho, C.-C. Chang, S.-L. Chen, Heat pipe with PCM for electronic cooling, Appl. Energy 88 (2011) 1825–1833.
[9] H. Nazir, M. Batool, F.J.B. Osorio, M. Isaza-Ruiz, X. Xu, K. Vignarooban, P. Phelan, A.M. Kannan, Recent developments in phase change materials for energy storage applications: a review, Int. J. Heat Mass Tran. 129 (2019) 491–523.
[10] Y. Lin, Y. Jia, G. Alva, G. Fang, Review on thermal conductivity enhancement, thermal properties and applications of phase change materials in thermal energy storage, Renew. Sustain. Energy Rev. 82 (2018) 2730–2742.
[11] N. Bondareva, M. Sheremet, Numerical simulation OF natural convection melting IN 2D and 3D enclosures, J. Therm. Eng. 5 (2019) 51–61.
[12] N. Bondareva, M. Sheremet, Numerical investigation of the two-dimensional natural convection inside the system based on phase change material with a source of volumetric heat generation, Thermophys. Aeromechanics 25 (2018) 525–537.
[13] L. Kumar, B. Manjunath, R. Patel, S. Markandeya, R. Agrawal, A. Agrawal, Y. Kashyap, P. Sarkar, A. Sinha, K. Iyer, Experimental investigations on melting of lead in a cuboid with constant heat flux boundary condition using thermal neutron radiography, Int. J. Therm. Sci. 61 (2012) 15–27.
[14] L. Kumar, B. Manjunath, R. Patel, S. Prabhu, Experimental investigations on melting of lead in a cuboid with constant heat flux boundary condition at two vertical walls using infra-red thermography, Int. J. Heat Mass Tran. 68 (2014) 132–140.

[15] O. Bertrand, B. Binet, H. Combeau, S. Couturier, Y. Delannoy, D. Gobin, M. Lacroix, P. Le Quéré, M. Médale, J. Mencinger, Melting driven by natural convection A comparison exercise: first results, Int. J. Therm. Sci. 38 (1999) 5–26.
[16] M. Bashar, K. Siddiqui, Experimental investigation of transient melting and heat transfer behavior of nanoparticle-enriched PCM in a rectangular enclosure, J. Energy Storage 18 (2018) 485–497.
[17] A.N. Keshteli, M. Sheikholeslami, Nanoparticle enhanced PCM applications for intensification of thermal performance in building: a review, J. Mol. Liq. 274 (2019) 516–533.
[18] M. Sheikholeslami, R.-u. Haq, A. Shafee, Z. Li, Heat transfer behavior of nanoparticle enhanced PCM solidification through an enclosure with V shaped fins, Int. J. Heat Mass Tran. 130 (2019) 1322–1342.
[19] M. Ghalambaz, A.J. Chamkha, D. Wen, Natural convective flow and heat transfer of Nano-Encapsulated Phase Change Materials (NEPCMs) in a cavity, Int. J. Heat Mass Tran. 138 (2019) 738–749.
[20] M. Ghalambaz, T. Groşan, I. Pop, Mixed convection boundary layer flow and heat transfer over a vertical plate embedded in a porous medium filled with a suspension of nano-encapsulated phase change materials, J. Mol. Liq. 293 (2019) 111432.
[21] N.S. Bondareva, B. Buonomo, O. Manca, M.A. Sheremet, Heat transfer performance of the finned nano-enhanced phase change material system under the inclination influence, Int. J. Heat Mass Tran. 135 (2019) 1063–1072.
[22] N.S. Bondareva, B. Buonomo, O. Manca, M.A. Sheremet, Heat transfer inside cooling system based on phase change material with alumina nanoparticles, Appl. Therm. Eng. 144 (2018) 972–981.
[23] M. Ghalambaz, A. Doostani, A.J. Chamkha, M.A. Ismael, Melting of nanoparticles-enhanced phase-change materials in an enclosure: effect of hybrid nanoparticles, Int. J. Mech. Sci. 134 (2017) 85–97.
[24] M. Ghalambaz, A. Doostani, E. Izadpanahi, A. Chamkha, Phase-change heat transfer in a cavity heated from below: the effect of utilizing single or hybrid nanoparticles as additives, J. Taiwan Inst. Chem. Eng. 72 (2017) 104–115.
[25] M. Sheikholeslami, A. Ghasemi, Z. Li, A. Shafee, S. Saleem, Influence of CuO nanoparticles on heat transfer behavior of PCM in solidification process considering radiative source term, Int. J. Heat Mass Tran. 126 (2018) 1252–1264.
[26] M. Sheikholeslami, M. Jafaryar, A. Shafee, Z. Li, Simulation of nanoparticles application for expediting melting of PCM inside a finned enclosure, Phys. Stat. Mech. Appl. 523 (2019) 544–556.
[27] K. Hosseinzadeh, M. Alizadeh, D. Ganji, Solidification process of hybrid nano-enhanced phase change material in a LHTESS with tree-like branching fin in the presence of thermal radiation, J. Mol. Liq. 275 (2019) 909–925.
[28] O. Mahian, L. Kolsi, M. Amani, P. Estellé, G. Ahmadi, C. Kleinstreuer, J.S. Marshall, M. Siavashi, R.A. Taylor, H. Niazmand, Recent advances in modeling and simulation of nanofluid flows-part I: fundamental and theory, Phys. Rep. 790 (2019) 1–48.
[29] O. Mahian, L. Kolsi, M. Amani, P. Estellé, G. Ahmadi, C. Kleinstreuer, J.S. Marshall, R.A. Taylor, E. Abu-Nada, S. Rashidi, Recent Advances in Modeling and Simulation of Nanofluid Flows-Part II: Applications, Physics Reports, 2018.
[30] S. Sivasankaran, A. Alsabery, I. Hashim, Internal heat generation effect on transient natural convection in a nanofluid-saturated local thermal non-equilibrium porous inclined cavity, Phys. Stat. Mech. Appl. 509 (2018) 275–293.
[31] M. Ghalambaz, A. Tahmasebi, A. Chamkha, D. Wen, Conjugate local thermal non-equilibrium heat transfer in a cavity filled with a porous medium: analysis of the element location, Int. J. Heat Mass Tran. 138 (2019) 941–960.
[32] M. Paknezhad, A. Rashidi, T. Yousefi, Z. Saghir, Effect of aluminum-foam heat sink on inclined hot surface temperature in the case of free convection heat transfer, Case Stud. Therm. Eng. 10 (2017) 199–206.
[33] M.A. Sheremet, I. Pop, Natural convection in a square porous cavity with sinusoidal temperature distributions on both side walls filled with a nanofluid: buongiorno's mathematical model, Transport Porous Media 105 (2014) 411–429.
[34] M.A. Ismael, H.S. Ghalib, Double diffusive natural convection in a partially layered cavity with inner solid conductive body, Sci. Iran. 25 (2018) 2643–2659.
[35] A. Alsabery, A. Chamkha, H. Saleh, I. Hashim, Natural convection flow of a nanofluid in an inclined square enclosure partially filled with a porous medium, Sci. Rep. 7 (2017) 2357.
[36] M.A. Ismael, Double-diffusive mixed convection in a composite porous enclosure with arc-shaped moving wall: tortuosity effect, J. Porous Media (2018) 21.
[37] N.S. Gibanov, M.A. Sheremet, M.A. Ismael, A.J. Chamkha, Mixed convection in a ventilated cavity filled with a triangular porous layer, Transport Porous Media 120 (2017) 1–21.
[38] X. Xiao, P. Zhang, M. Li, Preparation and thermal characterization of paraffin/metal foam composite phase change material, Appl. Energy 112 (2013) 1357–1366.
[39] H. Zheng, C. Wang, Q. Liu, Z. Tian, X. Fan, Thermal performance of copper foam/paraffin composite phase change material, Energy Convers. Manag. 157 (2018) 372–381.
[40] R. Hossain, S. Mahmud, A. Dutta, I. Pop, Energy storage system based on nanoparticle-enhanced phase change material inside porous medium, Int. J. Therm. Sci. 91 (2015) 49–58.
[41] M.S. Al-Jethelah, S.H. Tasnim, S. Mahmud, A. Dutta, Melting of nano-phase change material inside a porous enclosure, Int. J. Heat Mass Tran. 102 (2016) 773–787.
[42] A. Hussain, C. Tso, C.Y. Chao, Experimental investigation of a passive thermal management system for high-powered lithium ion batteries using nickel foam-paraffin composite, Energy 115 (2016) 209–218.
[43] M. Ghalambaz, J. Zhang, Conjugate solid-liquid phase change heat transfer in heatsink filled with phase change material-metal foam, Int. J. Heat Mass Tran. 146 (2020) 118832.
[44] Z. Ling, X. Wen, Z. Zhang, X. Fang, X. Gao, Thermal management performance of phase change materials with different thermal conductivities for Li-ion battery packs operated at low temperatures, Energy 144 (2018) 977–983.
[45] Z. Li, M. Sheikholeslami, M. Samandari, A. Shafee, Nanofluid unsteady heat transfer in a porous energy storage enclosure in existence of Lorentz forces, Int. J. Heat Mass Tran. 127 (2018) 914–926.
[46] P.T. Sardari, R. Babaei-Mahani, D. Giddings, S. Yasseri, M. Moghimi, H. Bahai, Energy recovery from domestic radiators using a compact composite metal Foam/PCM latent heat storage, J. Clean. Prod. 257 (2020) 120504.
[47] D.A. Nield, A. Bejan, Heat transfer through a porous medium, in: Convection in Porous Media, Springer, 2013, pp. 31–46.
[48] B. Buonomo, H. Celik, D. Ercole, O. Manca, M. Mobedi, Numerical study on latent thermal energy storage systems with aluminum foam in local thermal equilibrium, Appl. Therm. Eng. 159 (2019) 113980.
[49] P. Ranut, On the effective thermal conductivity of aluminum metal foams: review and improvement of the available empirical and analytical models, Appl. Therm. Eng. 101 (2016) 496–524.
[50] O. Mesalhy, K. Lafdi, A. Elgafy, K. Bowman, Numerical study for enhancing the thermal conductivity of phase change material (PCM) storage using high thermal conductivity porous matrix, Energy Convers. Manag. 46 (2005) 847–867.
[51] A. Bhattacharya, V.V. Calmidi, R.L. Mahajan, Thermophysical properties of high porosity metal foams, Int. J. Heat Mass Tran. 45 (2002) 1017–1031.
[52] R.W. Lewis, P. Nithiarasu, K.N. Seetharamu, Fundamentals of the Finite Element Method for Heat and Fluid Flow, John Wiley & Sons, 2004.
[53] J.N. Reddy, D.K. Gartling, The Finite Element Method in Heat Transfer and Fluid Dynamics, CRC press, 2010.
[54] J.C. De Los Reyes, S. González Andrade, A combined BDF-semismooth Newton approach for time-dependent Bingham flow, Numer. Methods Part. Differ. Equ. 28 (2012) 834–860.
[55] P. Wriggers, Nonlinear Finite Element Methods, Springer Science & Business Media, 2008.
[56] O. Schenk, K. Gärtner, Solving unsymmetric sparse systems of linear equations with PARDISO, Future Generat. Comput. Syst. 20 (2004) 475–487.
[57] F. Verbosio, A. De Coninck, D. Kourounis, O. Schenk, Enhancing the scalability of selected inversion factorization algorithms in genomic prediction, Journal of computational science 22 (2017) 99–108.
[58] A.C. Hindmarsh, P.N. Brown, K.E. Grant, S.L. Lee, R. Serban, D.E. Shumaker, C. S. Woodward, SUNDIALS: suite of nonlinear and differential/algebraic equation solvers, ACM Trans. Math Software 31 (2005) 363–396.
[59] C. Gau, R. Viskanta, Melting and solidification of a pure metal on a vertical wall, J. Heat Tran. 108 (1986) 174–181.
[60] S. Tiari, S. Qiu, M. Mahdavi, Numerical study of finned heat pipe-assisted thermal energy storage system with high temperature phase change material, Energy Convers. Manag. 89 (2015) 833–842.
[61] J. Khodadadi, S. Hosseinizadeh, Nanoparticle-enhanced phase change materials (NEPCM) with great potential for improved thermal energy storage, Int. Commun. Heat Mass Tran. 34 (2007) 534–543.
[62] S. Kashani, A. Ranjbar, M. Abdollahzadeh, S. Sebti, Solidification of nano-enhanced phase change material (NEPCM) in a wavy cavity, Heat Mass Tran. 48 (2012) 1155–1166.
[63] A. Brent, V.R. Voller, K. Reid, Enthalpy-porosity technique for modeling convection-diffusion phase change: application to the melting of a pure metal, Numer. Heat Tran. 13 (1988) 297–318.
[64] C. Beckermann, R. Viskanta, S. Ramadhyani, A numerical study of non-Darcian natural convection in a vertical enclosure filled with a porous medium, Numer. Heat Tran. 10 (1986) 557–570.
[65] A.C. Baytas, I. Pop, Free convection in oblique enclosures filled with a porous medium, Int. J. Heat Mass Tran. 42 (1999) 1047–1057.